

Article

# Research on Feature Extraction and Fault Diagnosis Method for Rolling Bearing Vibration Signals Based on Improved FDM-SVD and CYCBD

Jingzong Yang 

School of Dig Data, Baoshan University, Baoshan 678000, China; yjingzong@foxmail.com

**Abstract:** In mechanical equipment, rolling bearing components are constantly exposed to intricate and diverse environmental conditions, rendering them vulnerable to wear, performance degradation, and potential malfunctions. To precisely extract and discern rolling bearing vibration signals amidst intricate noise interference, this paper introduces a fault feature extraction and diagnosis methodology that seamlessly integrates an improved Fourier decomposition method (FDM), singular value decomposition (SVD), and maximum second-order cyclostationary blind convolution (CYCBD). Initially, the FDM is employed to meticulously decompose the bearing fault signals into numerous signal components. Subsequently, a comprehensive weighted screening criterion is formulated, aiming to strike a balance between multiple indicators, thereby enabling the selective screening and reconstruction of pertinent signal components. Furthermore, SVD and CYCBD techniques are introduced to carry out intricate processing and envelope demodulation analysis of the reconstructed signals. Through rigorous simulation experiments and practical rolling bearing fault diagnosis tests, the method's noteworthy effectiveness in suppressing noise interference, enhancing fault feature information, and efficiently extracting fault features is unequivocally demonstrated. Furthermore, compared to traditional time–frequency analysis methods such as EMD, EEMD, ITD, and VMD, as well as traditional deconvolution methods like MED, OMEDA, and MCKD, this method exhibits significant advantages, providing an effective solution for diagnosing rolling bearing faults in environments with strong background noise.



**Citation:** Yang, J. Research on Feature Extraction and Fault Diagnosis Method for Rolling Bearing Vibration Signals Based on Improved FDM-SVD and CYCBD. *Symmetry* **2024**, *16*, 552. <https://doi.org/10.3390/sym16050552>

Academic Editor: Jie Yang

Received: 26 March 2024

Revised: 18 April 2024

Accepted: 19 April 2024

Published: 3 May 2024



**Copyright:** © 2024 by the author. Licensee MDPI, Basel, Switzerland. This article is an open access article distributed under the terms and conditions of the Creative Commons Attribution (CC BY) license (<https://creativecommons.org/licenses/by/4.0/>).

**Keywords:** rolling bearing; Fourier decomposition method (FDM); singular value decomposition (SVD); maximum second-order cyclostationary blind convolution (CYCBD)

## 1. Introduction

As one of the critical moving components in mechanical equipment, rolling bearings find widespread application within various industries involving rotating machinery. Nevertheless, due to prolonged operational periods and the impact of working environments, rolling bearings often succumb to a range of faults, such as fatigue fractures, inadequate lubrication, and localized damage. If these faults are not promptly detected and diagnosed, they can lead to equipment downtime, damage, or even accidents, significantly hampering production efficiency and safety. Consequently, the investigation of rolling bearing fault diagnosis has consistently remained an essential and burgeoning topic within the field of mechanical engineering. The precise and rapid identification of fault features from rolling bearings holds substantial significance for predicting equipment lifespan, devising maintenance schedules, and enhancing equipment reliability [1,2].

In recent years, with the continuous advancement of signal processing and fault diagnosis techniques, an increasing number of methods have been proposed for extracting fault features from rolling bearings. Among these, time–frequency analysis methods play a crucial role in rolling bearing fault diagnosis [3]. The development of time–frequency analysis methods can be traced back to the 1940s [4] when Fourier analysis emerged as a

principal tool in signal processing [5,6]. Fourier analysis involves decomposing a signal into a series of superimposed sine and cosine functions, facilitating frequency–domain analysis of the signal. However, traditional Fourier analysis methods have difficulties in dealing with non-stationary and nonlinear signals effectively, whereas rolling bearing signals typically exhibit non-stationary and nonlinear characteristics. As a result, adaptive time–frequency analysis methods have emerged as suitable alternatives, offering more flexibility and accuracy in handling non-stationary and nonlinear signals. In recent years, numerous adaptive time–frequency analysis methods have been proposed and applied to rolling bearing fault feature extraction. Among these, methods such as empirical mode decomposition (EMD) [7], local mean decomposition (LMD) [8], and ensemble empirical mode decomposition (EEMD) [9] have achieved significant research progress in the realm of time–frequency analysis. Notably, EMD is a data-driven adaptive time–frequency analysis method that decomposes a signal into a series of intrinsic mode functions (IMFs), thereby extracting time-varying characteristics from the signal. LMD, on the other hand, decomposes a signal into local mean components and detail components, facilitating a time–frequency representation of the signal. EEMD, based on EMD, introduces random sampling to reduce mode-mixing effects and improve the precision of time–frequency analysis through multiple reconstructions. These methods have found widespread application in rolling bearing fault feature extraction. However, these methods often encounter challenges related to mode mixing and endpoint effects when dealing with non-stationary signals.

In recent years, the Fourier decomposition method (FDM) has emerged as a distinctive approach to handling non-stationary signals [10]. The FDM technique employs the Fourier transform to jointly analyze signals in both the frequency and time domains, decomposing them into fundamental frequency components and modulation functions. This combined analysis offers a more accurate depiction of signal time-varying characteristics, effectively avoiding mode mixing issues. Presently, this method has found applications across various domains. Karan Singh Parmar et al. [11] developed an automated diagnostic system for hypertension detection using electrocardiogram (ECG) signals. In their work, they applied the FDM to decompose ECG signals, followed by an assessment of signal transfer entropy and logarithmic energy entropy features. These features were subsequently used for classification in a classifier, yielding promising recognition outcomes. C. Dou et al. [12] substantiated through numerical analysis that the FDM overcomes the performance limitations of EMD in the adaptive separation of closely spaced frequency signal components. Moreover, by comparing the proposed method with conventional time–frequency analysis techniques, their results revealed its superior performance in characterizing vibration signals from turbine gearbox systems. Minqiang Deng et al. [13] introduced a fault diagnosis method for Gearboxes based on Resonance Bandwidth Fourier Decomposition (RBBFD). By comparison with existing techniques, they validated the superior performance of their method in gearbox fault diagnosis. Binish Fatimah et al. [14] proposed a recognition method for hand movements using surface electromyographic signals. Their approach involved the use of FDM to decompose signals, followed by the calculation of entropy, kurtosis, and norms of each signal, which were then utilized for training a classification model. Through testing on the UCI dataset and NinaPro DB5, their proposed method exhibited promising recognition results.

However, real-world mechanical systems often experience interference from strong background noise, posing challenges in accurate feature extraction and analysis of bearing faults. Traditional fault diagnosis methods perform poorly in such conditions, necessitating the need for more precise and effective technical solutions. Singular Value Decomposition (SVD), as a matrix decomposition technique [15,16], has been extensively applied in signal processing and data dimensionality reduction. SVD can decompose a signal into distinct singular values and corresponding singular vectors, thereby effectively removing noise components associated with smaller singular values and achieving signal denoising. Presently, the SVD method has been employed to extract useful features from signals in various domains, enhancing signal clarity and accuracy. Ren Y et al. [17] addressed the

difficulty in feature extraction from pressure fluctuation signals in tailwater pipes under a strong noise background by proposing a denoising method based on adaptive local iterative filtering (ALIF) and SVD. Evaluation through simulation experiments demonstrated that the ALIF-SVD denoising approach effectively eliminated noise while preserving useful signal information. Zhong C et al. [18] presented a rolling bearing radial basis neural network fault diagnosis method based on improved Ensemble Empirical Mode Decomposition-SVD (EEMD-SVD), validating its effectiveness through simulated bearing failure data. To suppress noise in atmospheric lidar echo signals, Cheng X et al. [19] proposed an Enhanced EEMD-SVD-Lifting Wavelet Transform (LWT) denoising algorithm. Comparative simulation experiments highlighted the superior denoising performance of the EEMD-SVD-LWT algorithm. Additionally, the CYCBD method, introduced by BUZZONI et al. [20] in 2018, as a second-order cyclic stationary blind deconvolution technique, has demonstrated exceptional performance in complex background noise scenarios. It has been applied to signal filtering and envelope demodulation analysis in fault diagnosis [21,22], enhancing the effectiveness of fault feature extraction.

Based on these considerations, this paper proposes a novel approach for fault feature extraction by combining improved FDM-SVD and CYCBD. First, the FDM technique is utilized to decompose bearing fault signals into a series of signal components. Subsequently, a fusion of kurtosis, skewness, and permutation entropy-based criteria is employed to select and reconstruct useful signal components. Next, Singular Value Decomposition (SVD) is applied to denoise the reconstructed signals. Finally, the CYCBD method is employed to filter the denoised signals, followed by envelope demodulation analysis. By synergistically leveraging the strengths of these methods, our aim is to overcome the interference of strong background noise in bearing fault signal analysis, thereby achieving more accurate and reliable fault feature extraction.

The main contributions of this study are as follows:

- (1) This paper introduces the application of FDM in decomposing the original signals. FDM not only divides the signals into different frequency components but also effectively eliminates adverse effects such as mode mixing. Through signal decomposition, we can gain a deeper understanding of the behavioral characteristics of bearings across various frequencies, thereby enabling a more accurate diagnosis of bearing faults. Furthermore, this study improves the selection mechanism for sensitive signal components by establishing a comprehensive weighted screening criterion that balances the strengths and weaknesses of multiple indicators. This criterion avoids potential blindness in selecting and discarding signal components. By objectively evaluating each signal component obtained through time–frequency analysis, we select the optimal signal components, which can address potential issues of insufficient extraction of bearing fault feature information and enhance the accuracy of fault diagnosis.
- (2) In this study, the Maximum Second-Order Cyclostationary Blind Convolution (CYCBD) method is employed to filter the signals after noise reduction through Singular Value Decomposition (SVD). This approach effectively highlights the periodic impact components within the signals, enabling us to extract the characteristic frequencies of bearing faults more clearly. This processing technique provides novel insights into the field of signal processing and enriches the theoretical and technological framework of the discipline.

The structure of this paper is as follows: Section 2 introduces the fundamental principles of improved FDM, SVD, and CYCBD algorithms. Section 3 delineates the specific implementation steps of the proposed methodology. Section 4 validates the effectiveness of the proposed approach through simulation experiments. Section 5 verifies the effectiveness of the proposed approach through actual bearing operation data. Section 6 presents the discussion and conclusion.

## 2. Theoretical Background

### 2.1. Improved Fourier Decomposition Method

The FDM algorithm comprises the LTH (Low to High) method, which involves searching from low to high frequencies, and the HTL (High to Low) method, which involves searching from high to low frequencies [23–25]. Essentially, the effectiveness of these two methods is indistinguishable, as both perform searches across the entire sampling frequency spectrum. The only distinction lies in the order of searching, whether it is from low to high frequencies or vice versa. Consequently, this paper solely focuses on elaborating the LTH algorithm. The FDM algorithm adaptively explores the Fourier Intrinsic Bandpass Functions (AFIBFs) throughout the entire Fourier domain, yielding numerous AFIBFs and a residual component. Among these, the AFIBFs satisfy the subsequent conditions:

- (1) The FIBF has a zero mean, i.e.:  $\int_a^b y_i(t)dt = 0$ .
- (2) The individual components of the FIBF are mutually orthogonal, i.e.:  $\int_a^b y_i(t)y_j(t)dt = 0$ ,  $i \neq j$ .
- (3) The analytical form of the FIBF,  $y_i(t)\hat{y}_j(t) = a_i(t)e^{j\varphi_i(t)}$ , possesses non-negative instantaneous amplitude and instantaneous frequency. Where  $a_i(t) \geq 0$ ,  $\varphi'_i(t) \geq 0$ ,  $\forall t \in [a, b]$ .  $y_i(t) \in C^\infty[a, b]$ . Therefore, the FIBF constitutes a summation of zero-mean sinusoidal functions with continuous frequency bands.

By defining the FIBF, the primary procedure of this algorithm is as follows:

- (1) Perform a fast Fourier transform on the signal  $x(n)$ ,  $X[k] = FFT\{[x(n)]\}$ ;
- (2) Scan through the AFIBF from low to high frequencies:

$$AFIBF = \sum_{k=N_{i-1}+1}^n X[k]\sigma^{\frac{j2\pi kn}{N}} = a_i(n)e^{j\varphi_i[n]} \quad (1)$$

The approach is devised to acquire the minimal number of *AFIBF* components from the signal. For each *AFIBF* component, denoted as *AFIBFi*, the process initiates from  $N_{i-1} + 1$  and incrementally accumulates components until the maximum number is achieved, all while satisfying the specified assumptions for the *AFIBFi* component of the signal. In this framework, specific parameters are assigned:  $N_0 = 0$  and  $N_M = (N/2 - 1)$ . These parameters are constrained by the requirement that  $N_{i-1} + 1 \leq N_i \leq (N/2 - 1)$ , and they adhere to the subsequent relationships:

$$a_i(t) \geq 0, \omega_i(t) = \frac{\varphi_i[n+1] - \varphi_i[n-1]}{2} \geq 0, \forall t \quad (2)$$

Due to its foundation in Fourier transform-based signal processing, the FDM presents a more comprehensive theoretical underpinning in contrast to EMD. In the pursuit of different frequency bands, the FDM achieves a dual fulfillment of both localized behavior and orthogonality.

The signals obtained through the FDM for adaptive decomposition effectively reduce the issues of mode-mixing and endpoint effects. However, these components may still include certain false components or components with low correlation to the original signals. To tackle the issue of inadequate extraction of fault characteristic information resulting from the blind selection or rejection of component signals, this study proposes a signal component selection combination criterion based on kurtosis, skewness, and permutation entropy on the basis of the original FDM algorithm. In the context of bearing fault signals, transient impacts are often present. Kurtosis is a temporal parameter that reflects the strength of transient impacts in a signal and is highly sensitive to such impact features. For signals with a higher proportion of impact components, their kurtosis values tend to be higher. Skewness, as a dimensionless parameter, quantifies the direction and degree of asymmetry in statistical data distribution, providing a numerical measure of distribution asymmetry. When a bearing has a fault, the periodic impulses caused by the fault lead to changes in the vibration signal. As a result, the skewness and kurtosis values increase.

Generally, larger skewness and kurtosis values indicate a greater presence of abnormal signals during the operational process. The calculation formulas for kurtosis and skewness are as follows:

$$Kurtosis_i = \frac{1}{\mu} \sum_{i=1}^n \left( \frac{\theta_i - \bar{x}}{\ell} \right)^4 \quad (3)$$

$$Skew_i = \frac{1}{\mu} \sum_{i=1}^n \left( \frac{\theta_i - \bar{x}}{\ell} \right)^3 \quad (4)$$

In Formulas (3) and (4),  $\theta_i$  and  $\bar{x}$  are the actual and average values of the original vibration signal.  $\ell$  is the standard deviation of the signal and  $\mu$  is the number of samples.

Meanwhile, the permutation entropy (PE) serves as a method for assessing the randomness and dynamical transitions within time series data. Its notable attributes encompass computational simplicity, rapid processing, and robust resistance to external interferences. Thus, it is capable of accurately depicting the mutational characteristics of intricate time series patterns. The magnitude of permutation entropy directly captures the degree of stochasticity within bearing vibration signals. Inspired by Shannon's entropy concept, the permutation entropy for a collection of  $m$  distinct symbol sequences can be mathematically formulated as follows:

$$PE(m) = - \sum_{l=1}^m P_l \ln P_l \quad (5)$$

where  $P_l$  is a probability distribution, and  $P_l = 1/m!$ ,  $PE(m)$  will obtain the maximum value  $\ln(m!)$ .

In order to standardize the obtained numerical values, the computed skewness, kurtosis, and permutation entropy are subjected to a process of normalization. Normalization involves transforming the information of each parameter into a probability distribution within the range of 0 to 1. The dimensionless selection index for each component is determined by summing the normalized skewness, kurtosis, and permutation entropy, yielding the following equation:

$$\lambda_i = Kurtosis_i + Skew_i + PE_i \quad (6)$$

where  $Kurtosis_i$ ,  $Skew_i$ , and  $PE_i$  represent the dimensionless parameters obtained from the normalization of skewness, kurtosis, and permutation entropy for each component, respectively. By employing the selection index, which amalgamates the multi-parameter information related to the faulty bearings, and subsequently ranking the selection indices, appropriate node components are chosen for reconstruction based on the superiority of their selection indices.

## 2.2. Singular Value Decomposition

Suppose a set of noisy signals under measurement is denoted as  $x = \{x_1, x_2, \dots, x_N\}$ , which can be represented as  $x = S_d + \omega_d$   $d = 1, 2, \dots, N$ . Drawing upon the principles of phase space reconstruction, it is feasible to reconstruct the Hankel matrix as follows [26–28]:

$$H = \begin{bmatrix} x_1 & x_2 & \cdots & x_n \\ x_2 & x_3 & \cdots & x_{n+1} \\ \vdots & \vdots & \vdots & \vdots \\ x_m & x_{m+1} & \cdots & x_N \end{bmatrix} = S + W \quad (7)$$

In the above equations: the feature matrix is defined as  $H \in R^{m \times n}$ ,  $1 < n < N$ , and  $m = N + n - 1$ .

Performing singular value decomposition on yields

$$H = U \Sigma V^T \quad (8)$$

In the given equations, both matrices  $U \in \mathbb{R}^{m \times m}$  and  $V \in \mathbb{R}^{n \times n}$  are orthogonal matrices, while matrix  $\Sigma$  is a non-negative diagonal matrix with its main diagonal elements denoted by  $\lambda_i$  ( $i = 1, 2, \dots, k$ ). The parameter  $k$  represents the rank of matrix  $H$ , with the condition that  $\lambda_1 \geq \lambda_2 \geq \dots \geq \lambda_k \geq 0$ , and  $\lambda_i$  signifies the singular values of  $H$ .

The higher the number of nonzero values in matrix  $\lambda_i$ , the more complex the components of the signal and the larger the proportion of noise. Therefore, to enhance the signal-to-noise ratio, it is advisable to subject the signal to Singular Value Decomposition, setting the smaller  $\lambda_i$  values that characterize the noise to zero, followed by the inverse transformation to obtain a denoised one-dimensional signal. For precise denoising, the choice of an appropriate denoising order is crucial. Consequently, the concept of the singular value energy differential spectrum is introduced to depict abrupt changes in singular values. Its formulation is as follows:

$$b_i = \sigma_i^2 - \sigma_{i+1}^2, \quad i = 1, 2, \dots, q - 1 \quad (9)$$

The sequence  $b_i$ , composed of elements in set  $B = [b_1, b_2, \dots, b_{q-1}]$ , is referred to as the difference spectrum. The above formula illustrates the variation in singular value energy. When the difference between adjacent singular values is significant, the difference spectrum exhibits peaks. This phenomenon arises because the singular values of the vibration signal are predominantly represented by  $\sigma_i$  ( $i = 1, 2, \dots, s$ ), whereas noise has a minor impact on the singular values. Consequently, peaks emerge at the boundary between the signal and noise. The energy difference spectrum between neighboring orders demonstrates relatively stable fluctuations, leading to smaller spectral peaks. Hence, the peak point can be selected as the threshold point denoted as 'r'. The singular values corresponding to the vibration signal are positioned prior to point 'r', while those corresponding to noise are positioned after point 'r'.

### 2.3. CYCBD Method

The CYCBD method aims to extract fault characteristic signals from complex observational data. In other words, it aims to recover the input source signal  $s$  from the raw measured signal. The deconvolution process it employs can be represented as follows:

$$s = x \otimes h = (s_0 \otimes g) \otimes h \approx s_0 \quad (10)$$

In the given equation,  $s$  represents the estimated source signal,  $x$  denotes the measured signal,  $\otimes$  stands for the convolution operator,  $h$  corresponds to the inverse filter,  $s_0$  represents the input source signal, and  $g$  is the impulse response function. The aforementioned equations can be expressed in the following matrix form:

$$s = Xh \quad (11)$$

Further decompose it to the following form:

$$\begin{bmatrix} s[N-1] \\ \vdots \\ s[L-1] \end{bmatrix} = \begin{bmatrix} x[N-1] & \cdots & x[0] \\ \vdots & \vdots & \vdots \\ x[L-1] & \cdots & x[L-N-2] \end{bmatrix} \cdot \begin{bmatrix} h[0] \\ \vdots \\ h[N-1] \end{bmatrix} \quad (12)$$

where  $s$  represents a discrete signal;  $L$  is the length of signal  $s$ ;  $h$  denotes the inverse filter; and  $N$  represents the length of filter  $h$ . Therefore, the new second-order cyclostationarity index  $ICS_2$  can be expressed in the form of generalized Rayleigh entropy:

$$ICS_2 = \frac{h^H X^H W X h}{h^H X^H X h} = \frac{h^H R_{XW} X h}{h^H R_{XX} h} \quad (13)$$

where  $h^H$  is the conjugate transpose operation on  $h$ ;  $R_{XX}$  represents the correlation matrix;  $R_{XWX}$  represents the weighted correlation matrix; and the weighted matrix  $W$  can be represented as follows.

$$W = \text{diag}\left(\frac{p[|s|^2]}{s^H s}\right)(L - N + 1) \quad (14)$$

$$p[|s|^2] = \frac{EE^H |s|^2}{L - N + 1} \quad (15)$$

$$|s|^2 = [s|N - 1|^2, \dots, s|L - 1|^2]^T \quad (16)$$

$$E = \begin{bmatrix} e^{-j2\pi\frac{1}{T}(N-1)} & \dots & e^{-j2\pi\frac{K}{T}(N-1)} \\ \vdots & \vdots & \vdots \\ e^{-j2\pi\frac{1}{T}(L-1)} & \dots & e^{-j2\pi\frac{K}{T}(L-1)} \end{bmatrix} \quad (17)$$

where  $N$  is the length of the source signal;  $L$  is the filtering length;  $K$  is the number of samples; and  $T$  is the failure cycle.

The concept of cyclic frequency is proposed in the CYCBD algorithm [29–32], which refers to the frequency related to an unknown energy fluctuation of the signal under cyclostationary conditions and is closely related to physical phenomena such as gear and bearing failures.

$$\alpha = k/T \quad (18)$$

From the properties of Rayleigh entropy, it can be inferred that the  $ICS_2$  maximization problem is equivalent to the eigenvalue maximization  $\mu$  of Rayleigh entropy as follows:

$$R_{XWX}h = R_{XX}h\mu \quad (19)$$

### 3. The Process of Fault Feature Extraction

Based on the specific steps of the fault feature extraction method, utilizing Improved FDM-SVD and CYCBD is as follows. The procedure for fault feature extraction is illustrated in Figure 1.

Step 1: Input the mechanical vibration signal and set the initialization parameters for the FDM algorithm. Subsequently, decompose the signal using the FDM to obtain several Frequency Interval Band Function (FIBF) components ordered from high to low frequencies.

Step 2: Compute the kurtosis, skewness, and permutation entropy of each signal component. Based on these statistics, determine the selection index for each of the components.

Step 3: Conduct a comparative analysis of the selection indices from all signal components. Choose the signal components with significantly larger selection indices for signal reconstruction.

Step 4: Apply singular value decomposition (SVD) denoising to the reconstructed signals.

Step 5: Perform CYCBD filtering on the denoised signals, followed by Hilbert envelope spectrum analysis, to extract fault features.

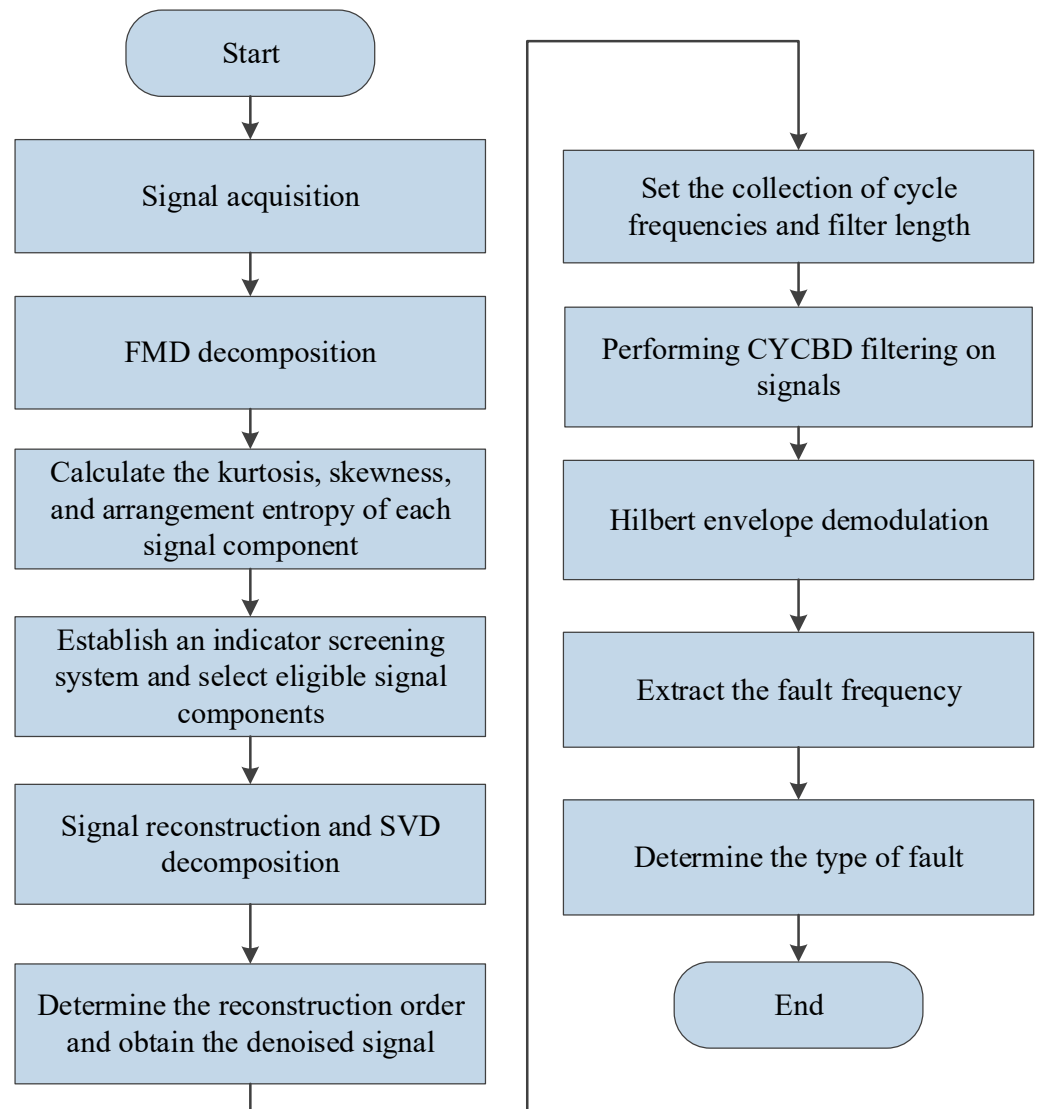


**Figure 1.** Flow chart of the proposed method.

#### 4. Simulation Verification

In order to verify the rationality of the method proposed in this study, simulation signals simulating the vibration of rolling bearings were introduced for experiments. The expression of this signal is as follows:

$$s(t) = y_0 e^{-2\pi f_n \zeta t} \sin(2\pi f_n \sqrt{1 - \zeta^2} t) \quad (20)$$

where the displacement constant  $y_0 = 5$ ; the carrier frequency  $f_n = 3000$  Hz; the damping ratio  $\zeta = 0.1$ ;  $f_s = 20$  kHz;  $t$  represents the sampling time, with a period  $T = 0.01$  s; the number of sampling points is  $N = 4096$ ; and the fault frequency  $f_0 = 100$  Hz.

To simulate a bearing fault in accordance with real-world scenarios, noise exhibiting a signal-to-noise ratio of  $-10$  dB was introduced into the aforementioned simulated signal. The simulation and analysis were conducted using MATLAB software (R2009a). The temporal domain representation of the generated simulation signal is depicted in Figure 2a. When the signal-to-noise ratio (SNR) is  $-10$  dB, as shown in Figure 2b, it can be observed that due to the influence of strong background noise, the periodic characteristics of the temporal signal waveform have been masked. Consequently, valuable fault information

cannot be identified from the temporal domain representation. Thus, further signal analysis is imperative.

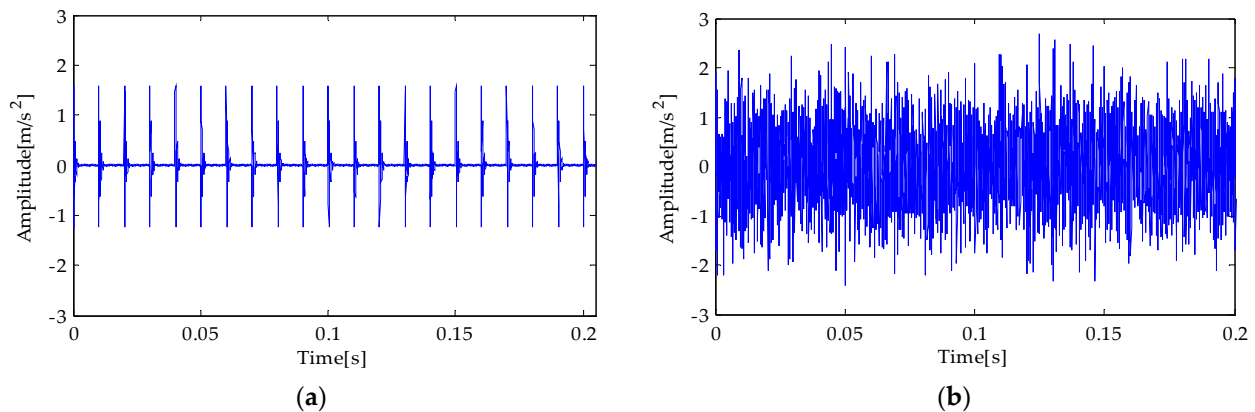


**Figure 2.** (a) Simulated signal; (b) simulated signal with noise.

The subsequent step involves the FDM analysis of the simulated signals after the introduction of noise. Following signal decomposition, a total of 35 signal components and the ultimate residual component are obtained. The decomposition results of the FDM are illustrated in Figure 3. Due to constraints on the article's length, only the decomposition outcomes of the first 20 signal components are presented. From the illustration, it is evident that this method effectively suppresses modal aliasing phenomena and substantially mitigates endpoint effects. To underscore the superiority of the fault diagnosis approach proposed in this paper, a comparative analysis is conducted against traditional methods. Specifically, the simulated noisy signals are subjected to EMD, EEMD, ITD, and VMD decompositions. The decomposition results of EMD, EEMD, ITD, and VMD are shown in Figure 4a–d, respectively. The analysis of the decomposition results of EMD and EEMD reveals that after EMD decomposition, 12 intrinsic mode functions (IMFs) and 1 residual component were obtained. Through EEMD decomposition, 11 IMFs and 1 residual component were derived. Notably, both methods exhibited instances of mode mixing in their decomposition results. Additionally, the decomposition using the ITD method yielded five PRC components and one residual component, while the VMD method produced six IMF components. After obtaining the signal components through the time–frequency analysis method, further calculations were performed to determine the kurtosis, skewness, and permutation entropy of each signal component. Subsequently, the filtering indices for these signal components were derived.

Tables 1–5 present the calculated comprehensive screening indices for all signal components obtained using FDM, EMD, EEMD, ITD, and VMD methods, respectively. A comparative analysis of the indices for the 35 signal components obtained through FDM in Table 1 reveals that the indices for the 20th, 21st, and 23rd signal components are significantly higher than those of the other components, making them suitable for signal reconstruction. Similarly, a comparison of the indices for the 12 signal components derived from EMD decomposition in Table 2 demonstrates that the index value for the second signal component is notably higher than the rest, thus selecting it for signal reconstruction. Furthermore, an examination of the indices for the 11 signal components obtained through EEMD decomposition in Table 3 indicates that the index value for the second signal component exceeds those of the other components, leading to its selection for signal reconstruction. Table 4 showcases the various PRC components derived from ITD decomposition, with the second signal component exhibiting the most significant index value among them, justifying its selection for signal reconstruction. Lastly, Table 5 presents the IMF components obtained through VMD decomposition. Among these, the fourth signal component stands out with the most prominent index value, thus chosen for signal reconstruction.

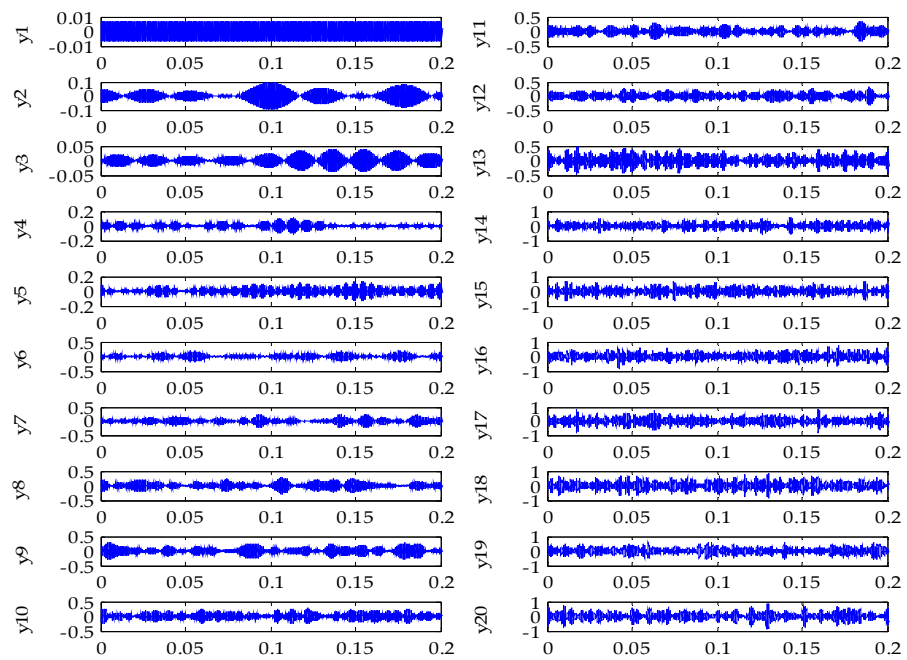


Figure 3. FDM decomposition result.

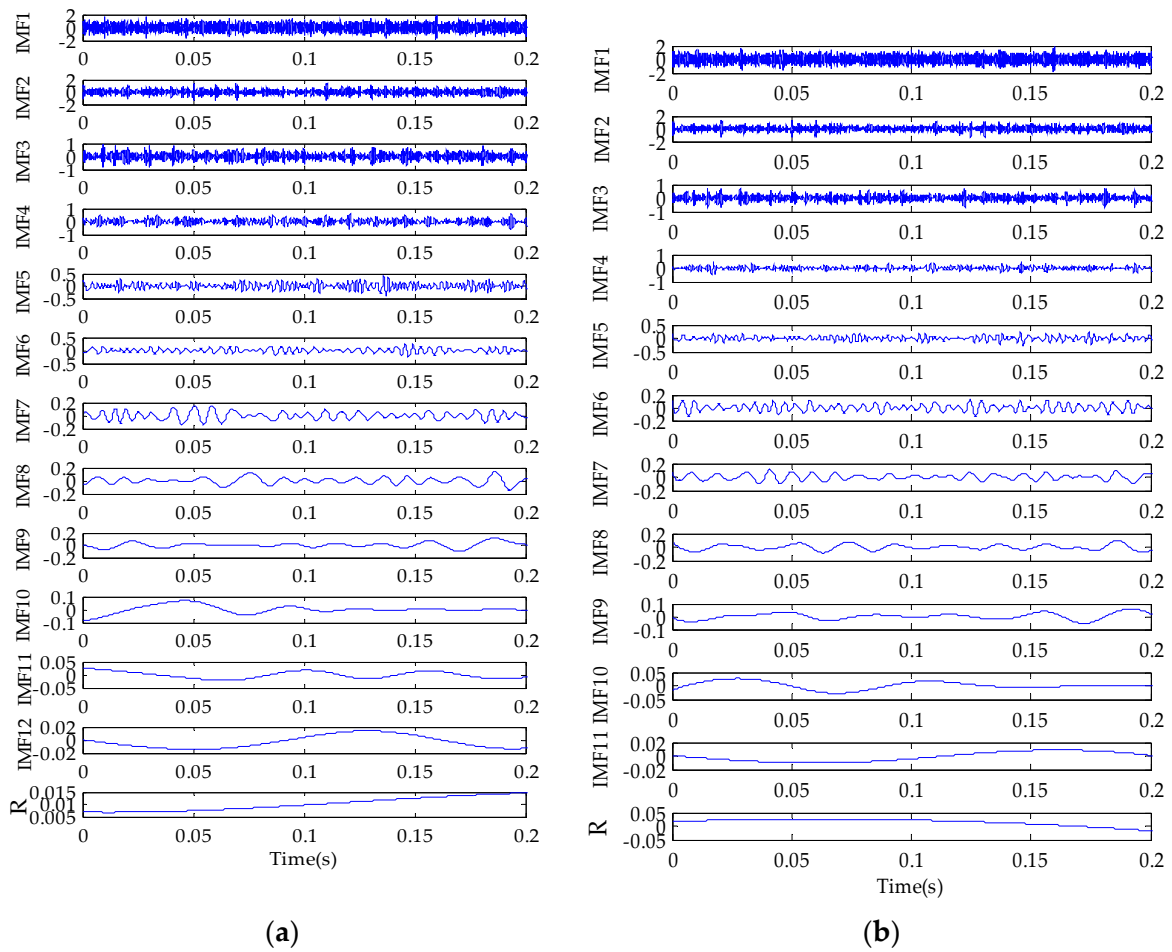


Figure 4. Cont.

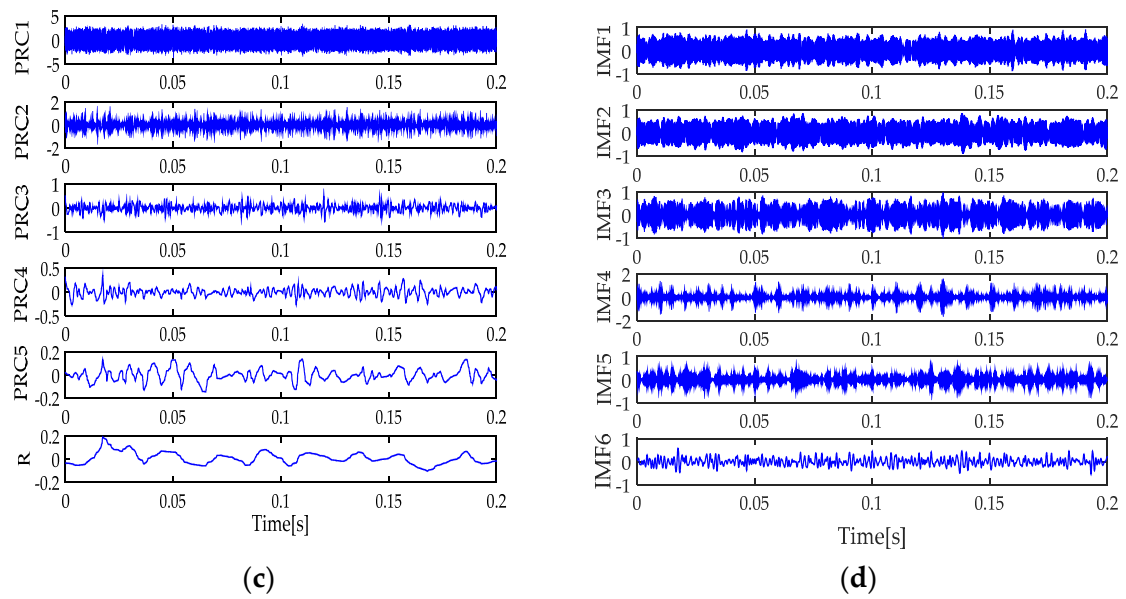


Figure 4. EMD (a), EEMD (b), ITD (c), and VMD (d) decomposition result.

Table 1. Indicator result value (FDM).

<b>y<sub>1</sub></b>	<b>y<sub>2</sub></b>	<b>y<sub>3</sub></b>	<b>y<sub>4</sub></b>	<b>y<sub>5</sub></b>	<b>y<sub>6</sub></b>	<b>y<sub>7</sub></b>	<b>y<sub>8</sub></b>	<b>y<sub>9</sub></b>	<b>y<sub>10</sub></b>
0.888	1.593	1.453	1.859	1.591	1.846	2.015	1.985	2.065	1.987
<b>y<sub>11</sub></b>	<b>y<sub>12</sub></b>	<b>y<sub>13</sub></b>	<b>y<sub>14</sub></b>	<b>y<sub>15</sub></b>	<b>y<sub>16</sub></b>	<b>y<sub>17</sub></b>	<b>y<sub>18</sub></b>	<b>y<sub>19</sub></b>	<b>y<sub>20</sub></b>
2.171	2.115	2.259	2.354	2.593	2.494	2.430	2.395	2.475	2.653
<b>y<sub>21</sub></b>	<b>y<sub>22</sub></b>	<b>y<sub>23</sub></b>	<b>y<sub>24</sub></b>	<b>y<sub>25</sub></b>	<b>y<sub>26</sub></b>	<b>y<sub>27</sub></b>	<b>y<sub>28</sub></b>	<b>y<sub>29</sub></b>	<b>y<sub>30</sub></b>
2.639	2.332	2.630	2.273	2.160	2.130	2.073	2.091	1.848	1.837
<b>y<sub>31</sub></b>	<b>y<sub>32</sub></b>	<b>y<sub>33</sub></b>	<b>y<sub>34</sub></b>	<b>y<sub>35</sub></b>					
1.816	1.520	1.468	1.169	0.000					

Table 2. Indicator result value (EMD).

<b>IMF<sub>1</sub></b>	<b>IMF<sub>2</sub></b>	<b>IMF<sub>3</sub></b>	<b>IMF<sub>4</sub></b>	<b>IMF<sub>5</sub></b>	<b>IMF<sub>6</sub></b>	<b>IMF<sub>7</sub></b>	<b>IMF<sub>8</sub></b>	<b>IMF<sub>9</sub></b>
1.426	1.891	1.557	1.389	1.026	0.782	0.891	0.881	1.356
<b>IMF<sub>10</sub></b>	<b>IMF<sub>11</sub></b>	<b>IMF<sub>12</sub></b>						
1.124	0.679	1.200						

Table 3. Indicator result value (EEMD).

<b>IMF<sub>1</sub></b>	<b>IMF<sub>2</sub></b>	<b>IMF<sub>3</sub></b>	<b>IMF<sub>4</sub></b>	<b>IMF<sub>5</sub></b>	<b>IMF<sub>6</sub></b>	<b>IMF<sub>7</sub></b>	<b>IMF<sub>8</sub></b>	<b>IMF<sub>9</sub></b>
2.146	2.835	2.346	2.312	1.728	1.390	1.352	1.467	1.644
<b>IMF<sub>10</sub></b>	<b>IMF<sub>11</sub></b>							
1.339	0.979							

Table 4. Indicator result value (ITD).

<b>PRC<sub>1</sub></b>	<b>PRC<sub>2</sub></b>	<b>PRC<sub>3</sub></b>	<b>PRC<sub>4</sub></b>	<b>PRC<sub>5</sub></b>
1.518	2.129	1.517	1.621	1.614

**Table 5.** Indicator result value (VMD).

IMF <sub>1</sub>	IMF <sub>2</sub>	IMF <sub>3</sub>	IMF <sub>4</sub>	IMF <sub>5</sub>	IMF <sub>6</sub>
0.553	1.133	0.531	1.867	0.574	1.329

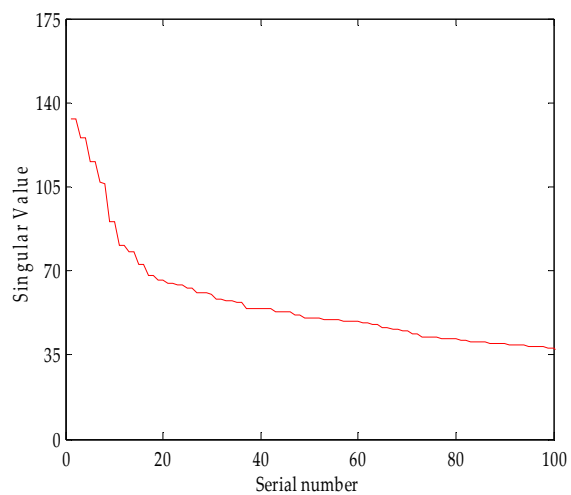
Subsequently, the component signals obtained through signal decomposition based on the FDM algorithm and constructed screening rules were reconstructed. Subsequently, the Hankel matrix was further constructed and subjected to SVD decomposition. The resulting singular value spectrum and singular value energy differential spectrum are presented in Figures 5 and 6, respectively. Figure 5a–e depicts the singular value distribution curves obtained through the FDM, EMD, EEMD, ITD, and VMD methods, respectively. It can be observed from the figures that, within the range of 1 to 100, the singular values continuously decrease and tend to stabilize as the sequence number increases.

Figure 6a–e present the singular value energy differential spectrum obtained using the FDM, EMD, EEMD, ITD, and VMD methods, respectively. As evident from Figure 6a, the energy of the 16th peak in the signal is relatively high, while subsequent peaks exhibit lower energy levels. Consequently, the reconstruction order corresponding to this peak is selected. Similarly, Figure 6b reveals that the energy of the 28th peak is significantly higher than the following peaks, prompting the selection of the reconstruction order associated with this peak. Likewise, Figure 6c indicates that the energy of the 22nd peak in the signal is relatively larger compared to subsequent peaks, leading to the selection of the corresponding reconstruction order. Figure 6d demonstrates that the energy of the 28th peak is relatively greater than subsequent peaks, justifying the choice of the corresponding reconstruction order. Finally, Figure 6e shows that the energy of the 18th peak stands out among subsequent peaks, thus justifying the selection of the reconstruction order corresponding to this peak.

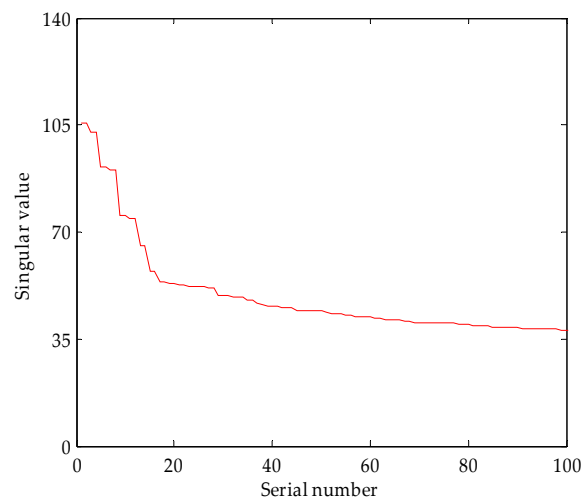
Figures 7–11 present the time-domain waveforms of signals denoised using five different methods: FDM, EMD, EEMD, ITD, and VMD. From these figures, we can clearly observe that each method effectively reduced varying degrees of noise interference after applying the SVD denoising technique. To accurately evaluate and compare the denoising effects of the above methods, this study employed quantitative analysis using assessment metrics such as the signal-to-noise ratio (SNR), cross-correlation coefficient, kurtosis, and Root Mean Square Error (RMSE). The relevant calculation results have been compiled in Table 6.

**Table 6.** Analysis of evaluation indicators.

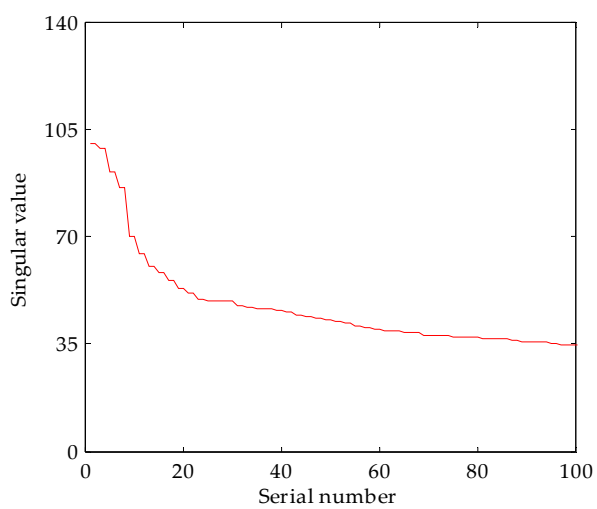
Evaluating Indicator	SNR	Correlation Coefficient	Kurtosis	RMSE
FDM	2.241	0.664	4.869	0.179
EEMD	1.856	0.560	4.518	0.187
EMD	1.772	0.599	4.511	0.189
ITD	0.248	0.269	2.846	0.226
VMD	1.623	0.574	4.005	0.193



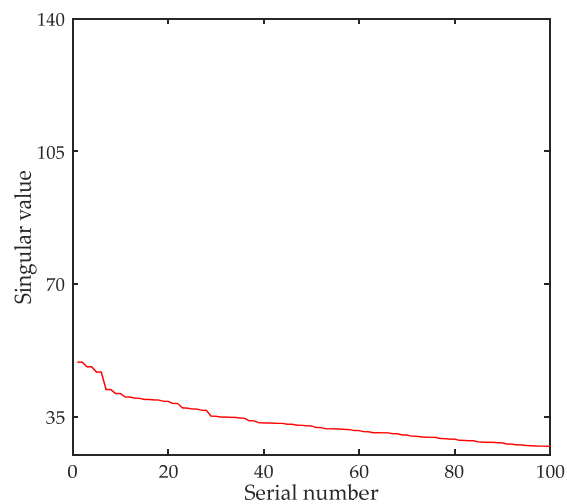
(a)



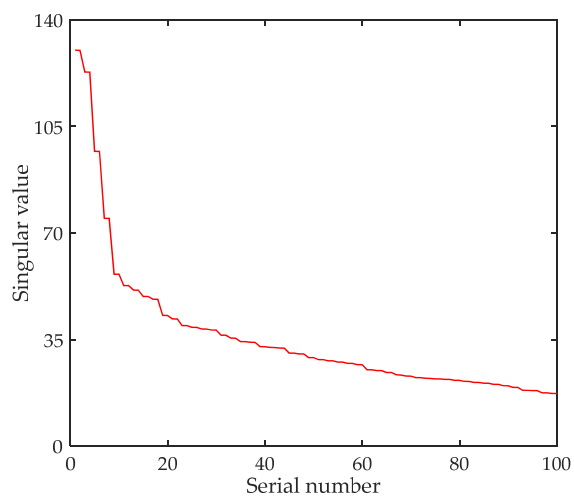
(b)



(c)



(d)



(e)

**Figure 5.** Signal singular value distribution curve of FDM (a), EMD (b), EEMD (c), ITD (d), and VMD (e).

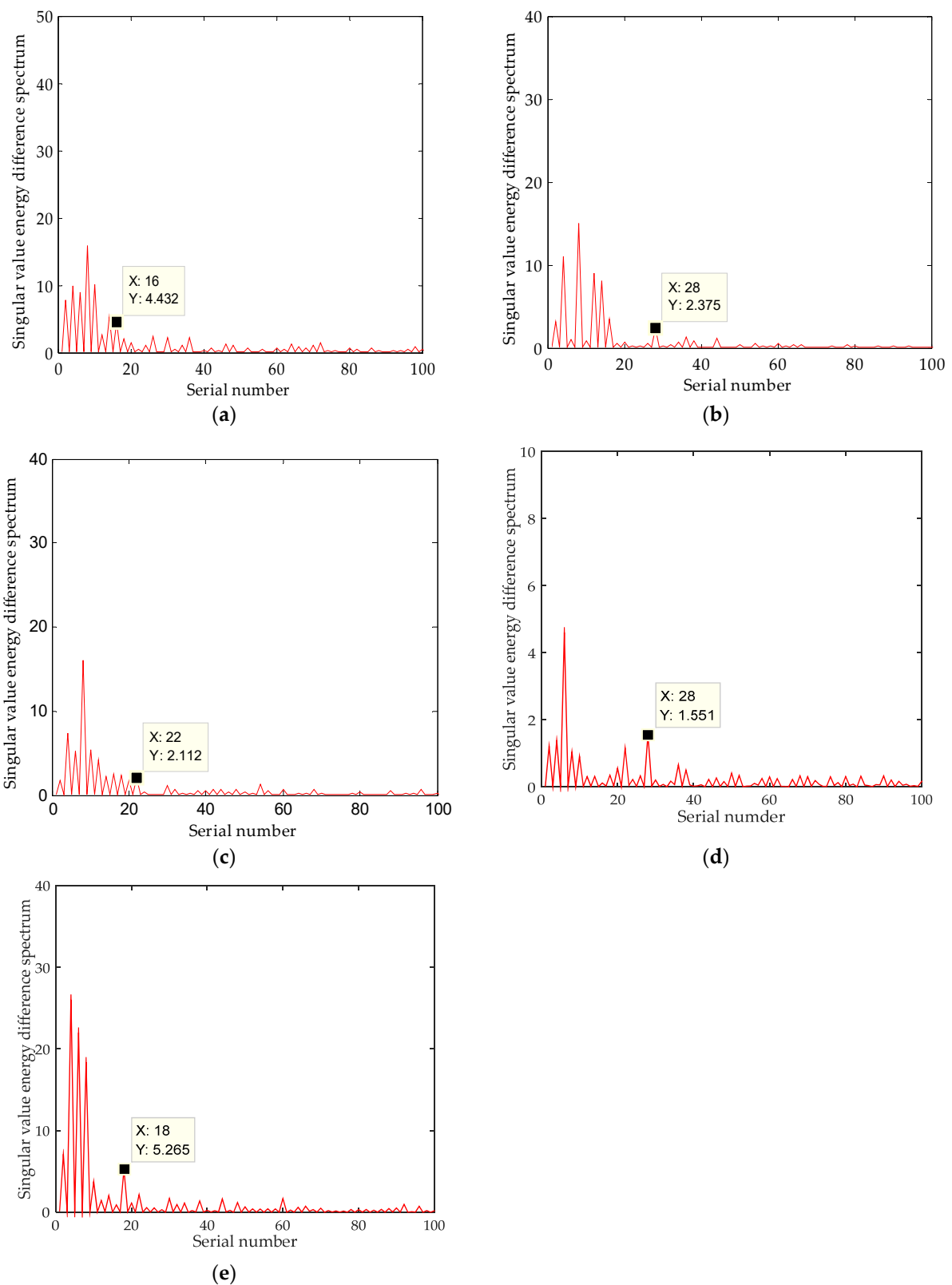


**Figure 6.** Singular value energy difference spectrum of FDM (a), EMD (b), EEMD (c), ITD (d), and VMD (e).

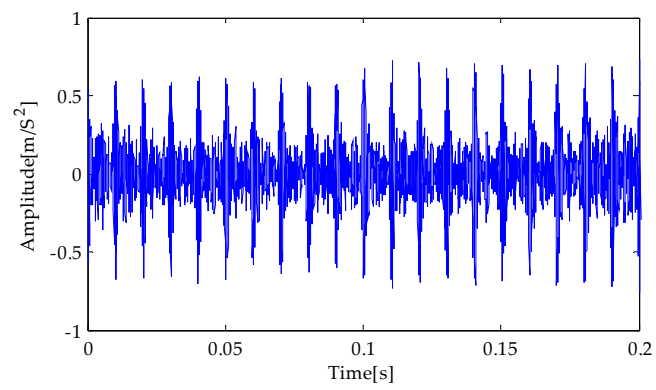


**Figure 7.** Signal after SVD denoising (FDM).

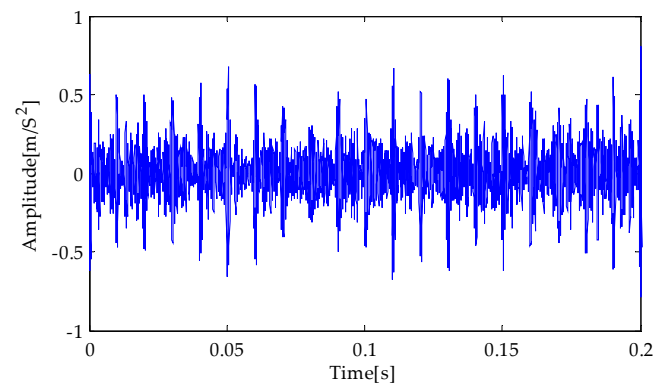


**Figure 8.** Signal after SVD denoising (EMD).

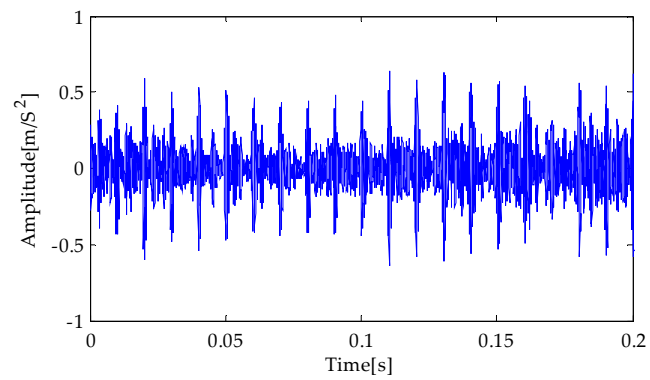


**Figure 9.** Signal after SVD denoising (EEMD).

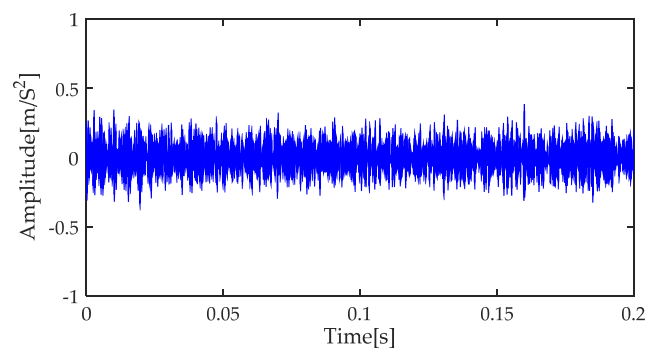


**Figure 10.** Signal after SVD denoising (ITD).

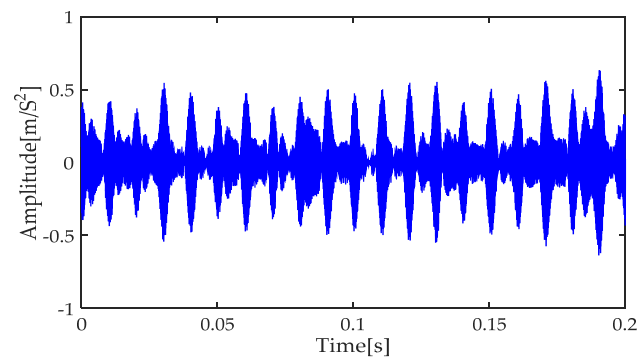


**Figure 11.** Signal after SVD denoising (VMD).

From Table 6, we can observe that after denoising the signal using the FDM-SVD method, the resulting signal-to-noise ratio (SNR) is 2.241, the cross-correlation coefficient is 0.664, the kurtosis value is 4.869, and the RMSE is 0.179. In contrast, for the EMD-SVD method, the corresponding values are 1.772, 0.599, 4.511, and 0.189, respectively. The EEMD-SVD method yields an SNR of 1.856, a cross-correlation coefficient of 0.560, a kurtosis value of 4.518, and a RMSE of 0.187. The corresponding values for the ITD-SVD method are 0.248, 0.269, 2.846, and 0.226. Lastly, the VMD-SVD method exhibits metric values of 1.623, 0.574, 4.005, and 0.193. Overall, the results obtained using the FDM-SVD method are relatively superior. To conduct a more comprehensive comparative analysis, this study proceeds to perform envelope spectrum analysis on the denoised signals obtained through these methods. The results are presented in Figures 12–16.

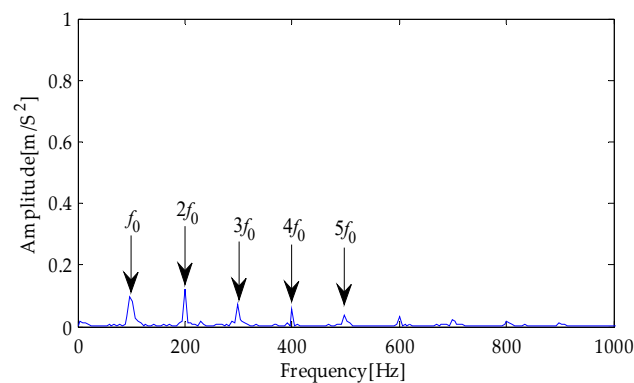


**Figure 12.** Envelope spectrum based on FDM-SVD.

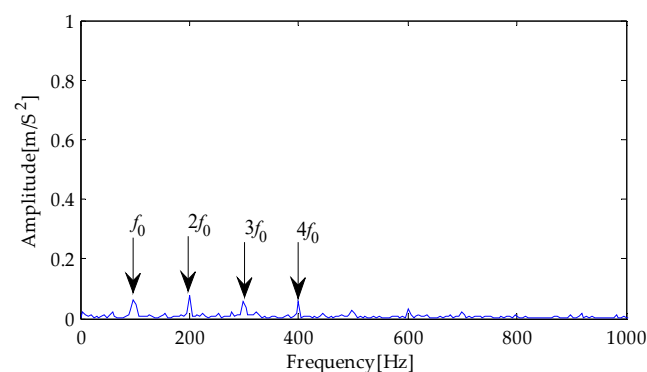


**Figure 13.** Envelope spectrum based on EMD-SVD.

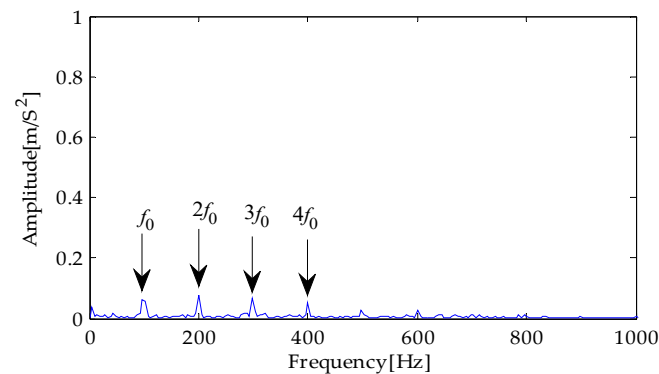


**Figure 14.** Envelope spectrum based on EEMD-SVD.

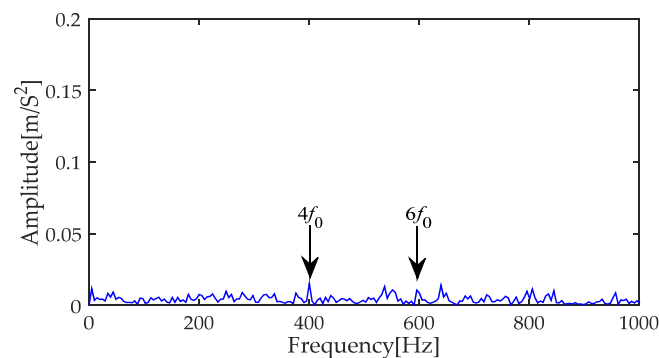


**Figure 15.** Envelope spectrum based on ITD-SVD.

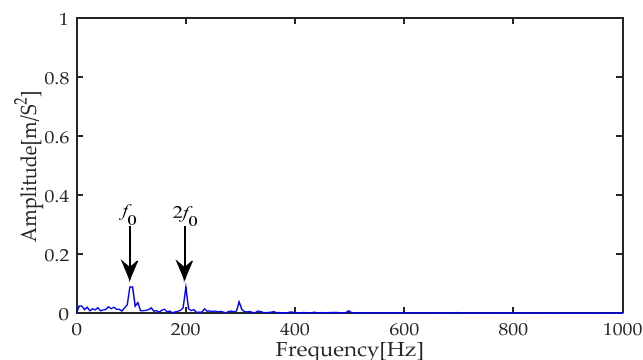


**Figure 16.** Envelope spectrum based on VMD-SVD.

The envelope spectrum obtained using five methods, namely FDM-SVD, EMD-SVD, EEMD-SVD, ITD-SVD, and VMD-SVD, are presented in Figures 12–16, respectively. A detailed analysis of these figures reveals that, after the process of signal time–frequency decomposition and noise reduction, all these methods can extract fault characteristic frequencies to varying degrees, albeit with the presence of irrelevant frequency interference. Additionally, the amplitudes of the extracted fault frequency peaks by other methods are relatively low. However, compared to the other methods, the FDM-SVD method exhibits superior performance in extracting fault characteristic frequencies and their multiples, with relatively higher peak values and reduced irrelevant interference near the fault frequencies.

To enhance the periodic impulse features in the signal, the noise-reduced signals obtained through FDM-SVD, EMD-SVD, EEMD-SVD, ITD-SVD, and VMD-SVD methods will be filtered using the CYCBD method. Subsequently, the Hilbert envelope spectra are generated. Figures 17–21 depict the envelope spectra obtained using the FDM-SVD-CYCBD, EMD-SVD-CYCBD, EEMD-SVD-CYCBD, ITD-SVD-CYCBD, and VMD-SVD-CYCBD methods, respectively. Analysis of these five methods reveals that after CYCBD filtering, all five methods can accurately extract the fault characteristic frequency and its multiples, ranging

from double to septuple frequencies. Notably, the amplitude of the fault characteristic frequency and its multiples extracted by the FDM-SVD-CYCBD method is the highest. Furthermore, the FDM-SVD-CYCBD method significantly reduces the influence of irrelevant frequency interference in the signal.

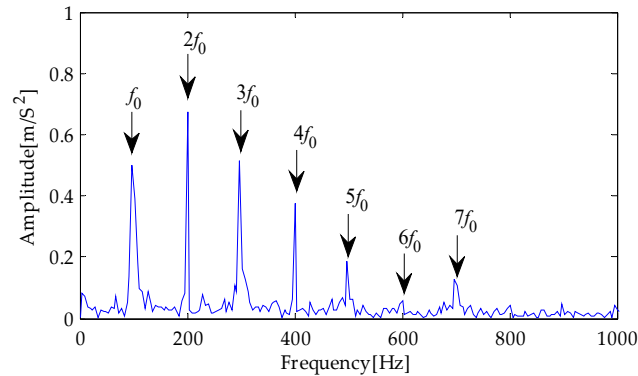


**Figure 17.** Envelope spectrum of CYCBD filter signal based on FDM-SVD.

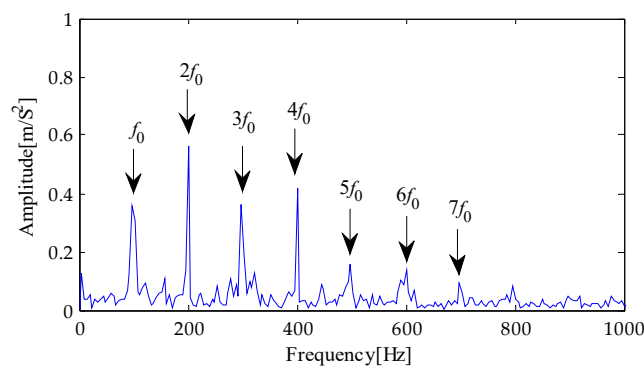


**Figure 18.** Envelope spectrum of CYCBD filter signal based on EMD-SVD.

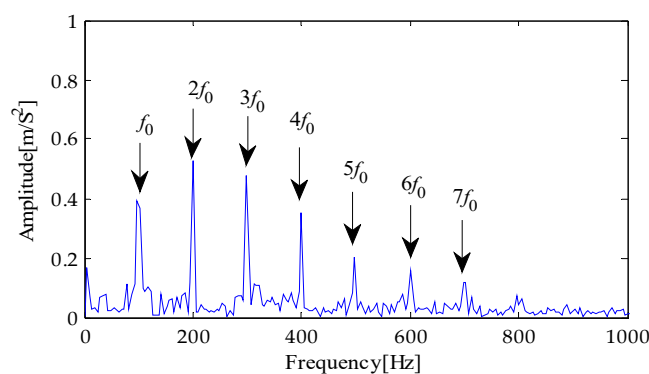


**Figure 19.** Envelope spectrum of CYCBD filter signal based on EEMD-SVD.

The vibration signal of a bearing can essentially be regarded as the convolution result of the source signal and channel characteristics. In signal processing, deconvolution, as a method to solve the inverse convolution filter, aims to restore the original source signal and remove the influence of the channel on the signal. Therefore, methods based on blind deconvolution theory have inherent advantages in noise reduction processing for bearing vibration signals. Other common methods include Minimum Entropy Deconvolution (MED), Maximum Kurtosis Deconvolution (MCKD), and Optimal Minimum Entropy Deconvolution Adjusted (OMEDA) [33–35]. To comprehensively and deeply compare the effectiveness of different deconvolution methods in signal filtering, this study combined FDM-SVD for signal preprocessing. Based on this, we applied MED, OMEDA,

and MCKD for filtering. Subsequently, Hilbert envelope spectra were generated and presented in Figures 22–24.

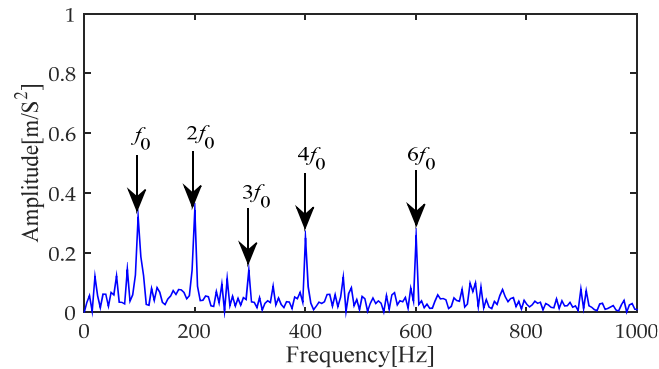


**Figure 20.** Envelope spectrum of CYCBD filter signal based on ITD-SVD.

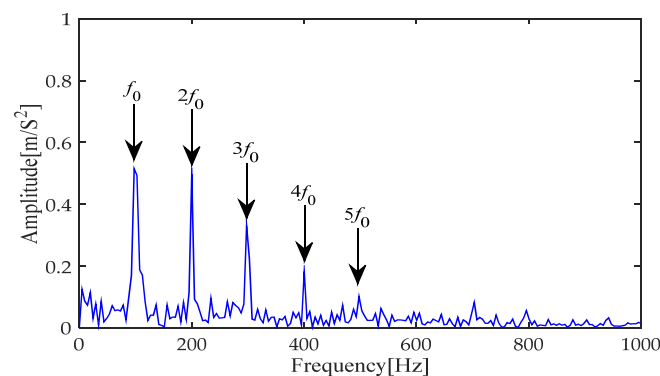


**Figure 21.** Envelope spectrum of CYCBD filter signal based on VMD-SVD.

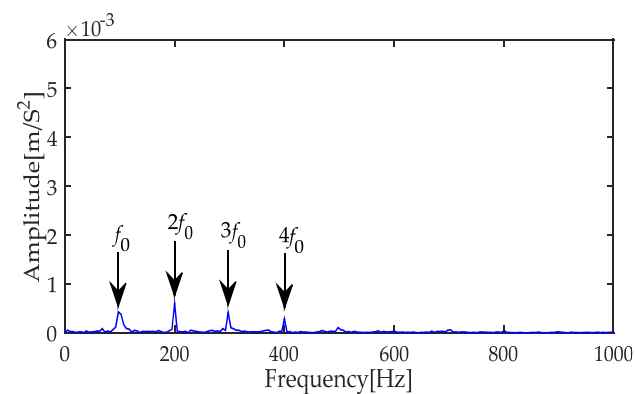


**Figure 22.** Envelope spectrum of signals filtered via MED.

Observing these three figures, it can be seen that although the envelope spectra obtained after filtering with the aforementioned deconvolution methods can extract fault characteristic frequencies, these frequencies often have low amplitudes and are susceptible to interference from other unrelated frequency components. This interference not only blurs the fault characteristics but also significantly hinders accurate fault diagnosis. To more objectively assess the performance of various methods, we listed the envelope spectrum sparsity values of the signals filtered using the above deconvolution techniques in Table 7. In the case of mechanical faults in bearings, discrete peaks in the vibration signal become particularly prominent, thereby significantly enhancing sparsity. The appearance of discrete peaks at specific frequencies in the envelope spectrum further increases sparsity, explicitly indicating the presence of different fault pulses in the signal.

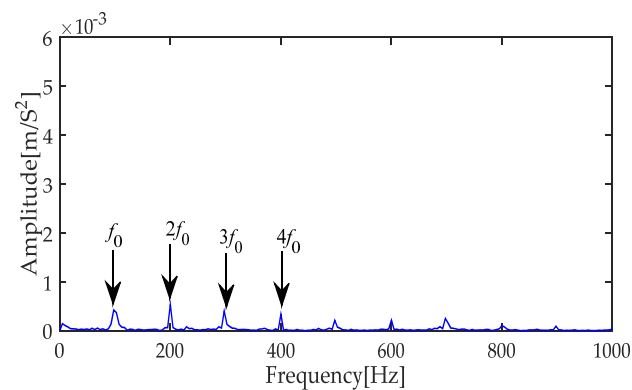


**Figure 23.** Envelope spectrum of signals filtered via OMEDA.

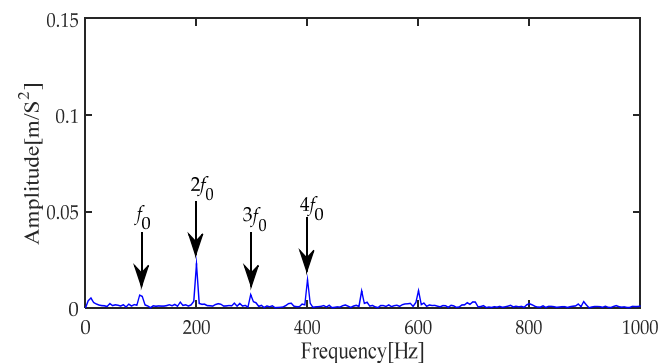


**Figure 24.** Envelope spectrum of signals filtered via MCKD.

**Table 7.** Spectrum sparsity of simulated signals by various methods.

CYCBD	MCKD	OMEDA	MED
0.0288	0.0252	0.0226	0.0227

Through comparative analysis of these results, it is evident that the envelope spectrum sparsity values after filtering with the CYCBD method are significantly higher than those of other methods, fully demonstrating the superior performance of CYCBD in signal filtering. It not only effectively extracts fault features but also significantly reduces interference from unrelated frequency components, providing more accurate and reliable data support for subsequent fault diagnosis. It is worth mentioning that the CYCBD algorithm, as a novel blind deconvolution method based on maximum second-order cyclic indices, exhibits unique advantages in the field of signal processing. As a robust and sensitive indicator, the cyclic stationarity index plays a crucial role in early fault detection and identification. Compared to traditional methods such as MED, MCKD, and OMEDA, CYCBD demonstrates stronger capability in fault feature extraction. Especially in scenarios with significant pulse noise, the deconvolution effect of CYCBD is more outstanding, effectively filtering out noise and highlighting fault features.

## 5. Experimental Verification

To validate the feasibility of the proposed method, we conducted an empirical analysis. The data used in this study were sourced from the publicly available dataset of the Case Western Reserve University (CWRU) laboratory [36]. The experimental setup is illustrated in Figure 25 [37]. The experiment involved driving a motor, which was equipped with a torque sensor and an encoder on the motor drive shaft. Torque was applied to the shaft through a dynamometer and electronic control system. SKF deep groove ball bearings were installed at both the drive end and the fan end. Various faults were artificially induced

at different locations of the bearings using electrical discharge machining to simulate different operating conditions of the rolling bearings. Throughout the experiment, the motor operated at a speed of 1797 rpm, with a sampling frequency of 12 kHz. The collected data consisted of vibration signals from the inner and outer races with a failure diameter of 0.007 inches.

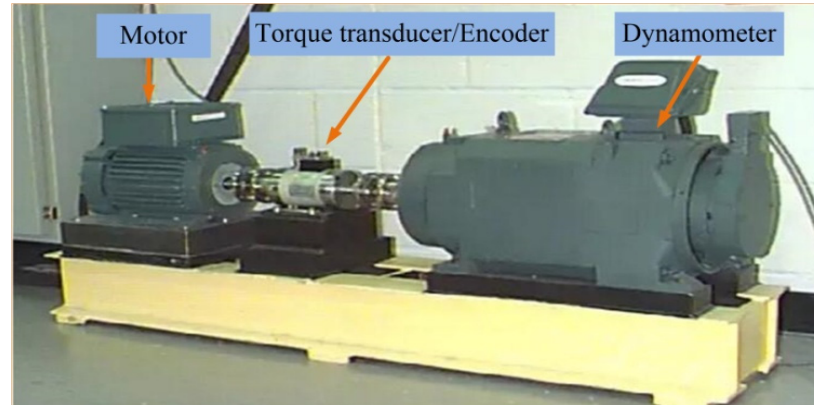


**Figure 25.** Fault acquisition equipment.

### 5.1. Inner Ring Signal Analysis

After processing the collected fault data, we obtained the time-domain waveform of the inner race fault signal of the rolling bearing, as shown in Figure 26. Upon observation of the waveform, it is evident that the noise interference in the signal is not prominent. To validate the effectiveness of the proposed method, we introduced Gaussian white noise with a signal-to-noise ratio of  $-5$  dB into the inner race fault signal, generating a composite signal. The time-domain waveforms of these composite signals are displayed in Figure 27. In Figure 27, it is noticeable that the addition of noise to the inner race fault signal results in a blurring of the impulsive features within the signal.

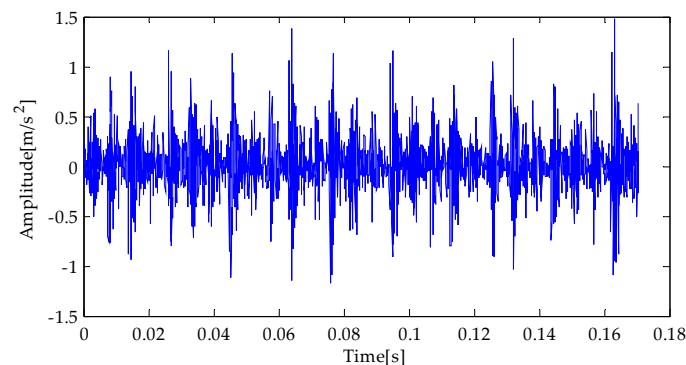


**Figure 26.** Time domain waveform of the inner ring fault signal.

Next, we conducted FDM analysis on the inner race fault composite signal with added noise. Through signal decomposition, we obtained 24 signal components and a final residual component. Due to space limitations, only the decomposition results of the first 20 signal components are shown in Figure 28. By examining the waveforms of these component signals, it can be observed that this method effectively suppresses modal aliasing, thereby avoiding interference between different frequency components. Additionally, endpoint effects have been largely eliminated, indicating that the signal maintains good stability and accuracy during the decomposition process.

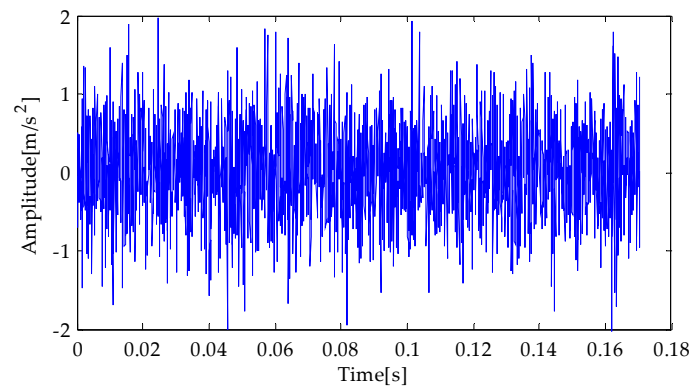


Figure 27. Time domain waveform of the mixed signal.

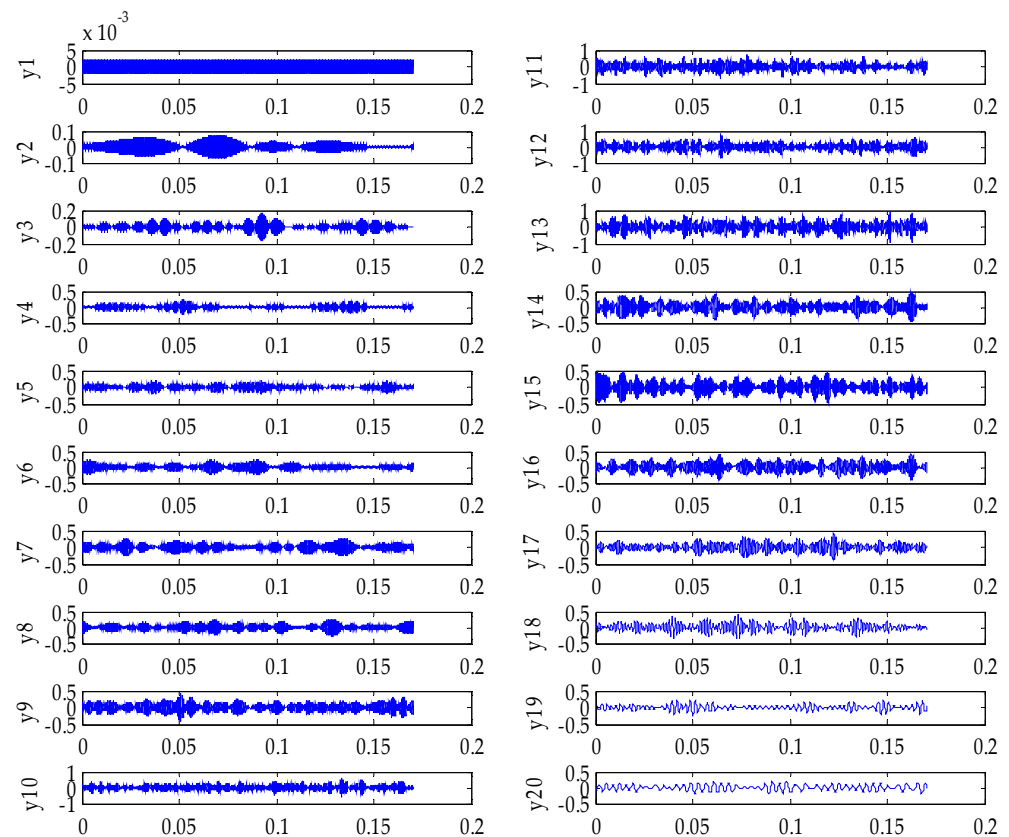


Figure 28. FDM decomposition result.

We proceeded with a detailed statistical feature analysis of each signal component, including computations of their kurtosis, skewness, and permutation entropy. Based on this analysis, we further derived a selection index for each signal component to assess their significance within the overall signal. Table 8 provides a comprehensive listing of the computed selection indices for all signal components. Upon careful comparison of the selection index values for the 24 components in the table, it becomes evident that Components 10, 11, and 13 exhibit markedly higher selection indices compared to the other components. This suggests that these three components hold a more prominent position within the overall signal, potentially encapsulating more significant fault information. Consequently, we chose to reconstruct the signal using these three selected components.

**Table 8.** Indicator result value (FDM).

	Y1	Y2	Y3	Y4	Y5	Y6	Y7	Y8	Y9	Y10
$\lambda$	0.272	0.929	1.541	1.505	1.422	1.696	1.660	1.760	1.685	2.074
	Y11	Y12	Y13	Y14	Y15	Y16	Y17	Y18	Y19	Y20
$\lambda$	2.097	1.857	2.034	1.981	1.970	1.697	1.854	1.858	1.684	1.188
	Y21	Y22	Y23	Y24						
$\lambda$	1.092	1.430	1.026	1.000						

Subsequently, we proceeded with the reconstruction of the component signals obtained through the signal decomposition based on the FDM algorithm and the applied selection criteria. Furthermore, we advanced to construct a Hankel matrix, followed by performing Singular Value Decomposition (SVD). The resulting singular value spectrum and the energy difference spectrum are depicted in Figures 29 and 30, respectively. Figure 30's energy difference spectrum of singular values illustrates the disparities in energy between them. Upon observation of this graph, it becomes evident that the 38th peak of the signal exhibits relatively higher energy compared to all subsequent peaks. Hence, we selected the reconstruction order corresponding to this peak.

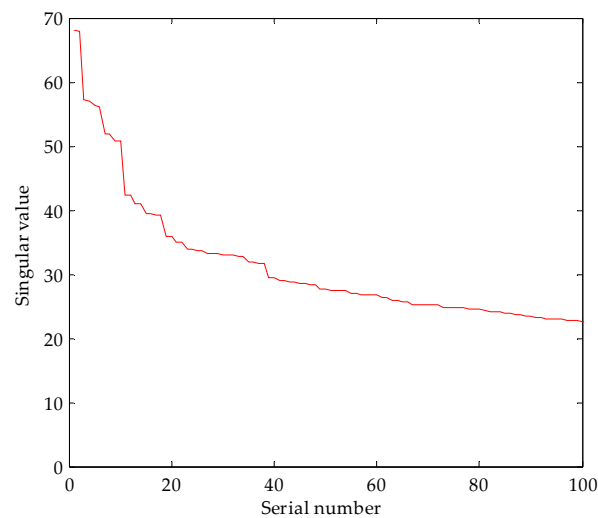
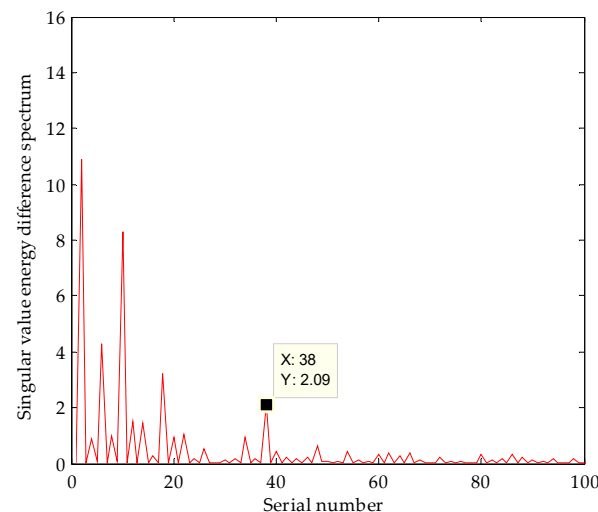
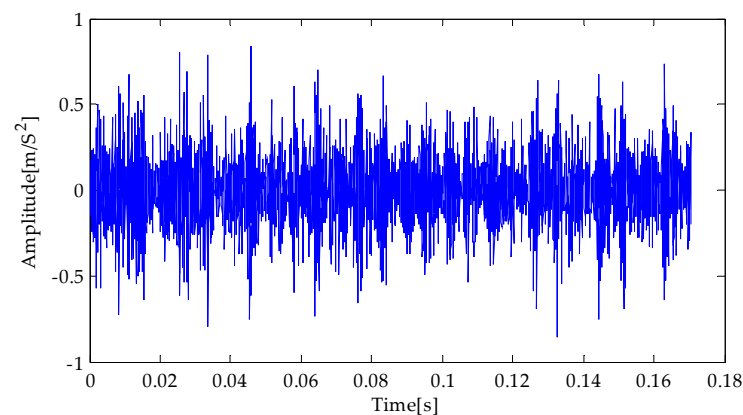
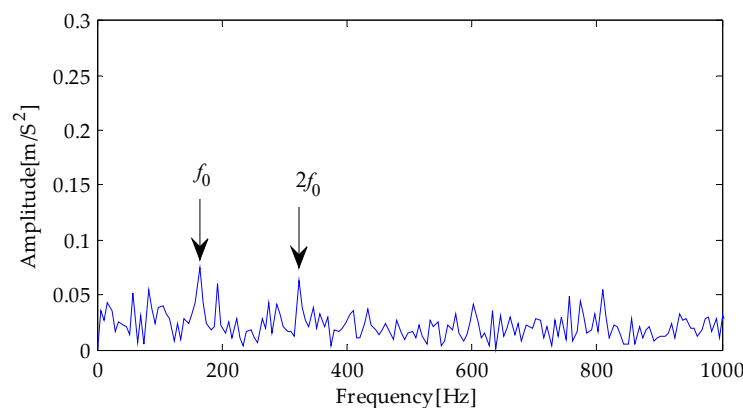
**Figure 29.** Signal singular value distribution curve.**Figure 30.** Singular value energy difference spectrum.

Figure 31 displays the time-domain waveform of the signal after denoising using the Singular Value Decomposition (SVD) method. Upon close examination of this figure, it is evident that the noise interference originally present in the signal has been substantially reduced through SVD denoising. This denoising process has enabled the emergence of impact components in the inner race fault signal, providing a more reliable foundation for subsequent fault analysis. Figure 32, on the other hand, illustrates the envelope spectrum obtained through Hilbert transformation. From this figure, we can extract the fundamental frequency and its second harmonic components of the inner race fault in the bearing. The presence of these components serves as crucial evidence for detecting inner race faults. However, the peak frequencies associated with the faults are relatively low, and there are numerous other irrelevant interferences in the envelope spectrum. These interferences might pose a certain level of difficulty in identifying fault harmonics.



**Figure 31.** Signal after SVD denoising.



**Figure 32.** Envelope spectrum based on FDM-SVD.

To highlight the periodic impact characteristics within the signal, the denoised signal obtained through the FDM-SVD method was fed into the CYCBD filter for further extraction of fault features. Finally, an envelope spectrum was generated through Hilbert transformation, as shown in Figure 33. Upon analysis of this figure, it is evident that after CYCBD filtering, the resulting envelope spectrum distinctly reveals multiple components corresponding to fault feature frequencies, including their second to sixth harmonics. These components are clearly manifested in the form of prominent peaks, facilitating observation and identification. Simultaneously, surrounding interference components are effectively suppressed during the CYCBD filtering process, thereby minimally affecting the identification of harmonics.

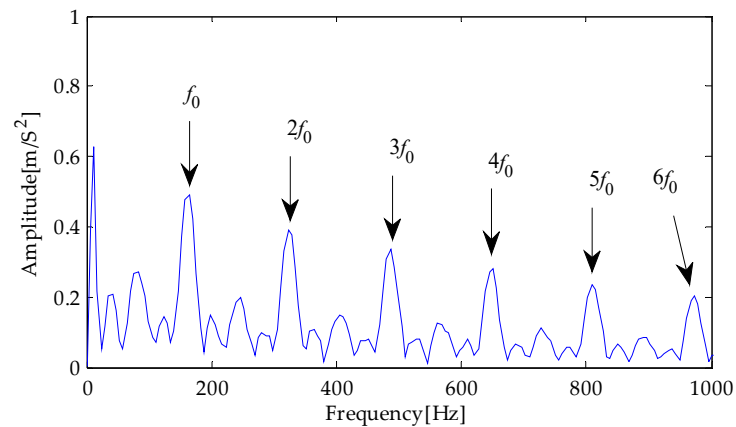


**Figure 33.** Envelope spectrum of CYCBD filter signal based on FDM-SVD.

### 5.2. Outer Ring Signal Analysis

By processing the collected fault data, we obtained the time-domain waveform of the outer race bearing fault signal, as shown in Figure 34. Upon waveform observation, it was also noted that the presence of noise interference in the signal was not significant. Therefore, in this experiment, Gaussian white noise with a signal-to-noise ratio of  $-5$  dB was added to the outer race fault signal, generating mixed signals. The time-domain waveforms of these mixed signals are shown in Figure 35. In Figure 35, it can be observed that the addition of noise to the outer race fault signal resulted in a blurring of the impulsive characteristics in the signal.

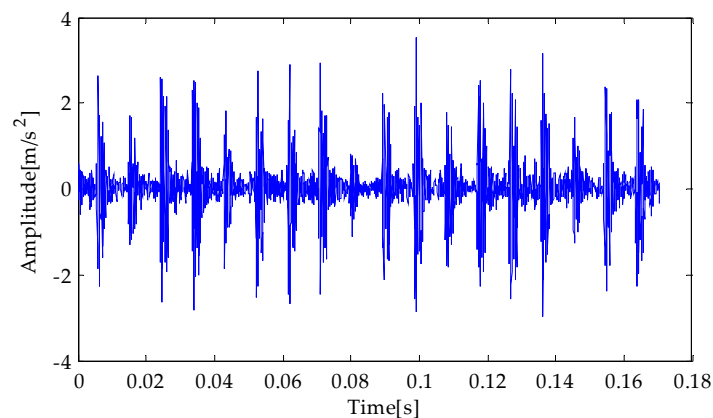


**Figure 34.** Time domain waveform of the outer ring fault signal.

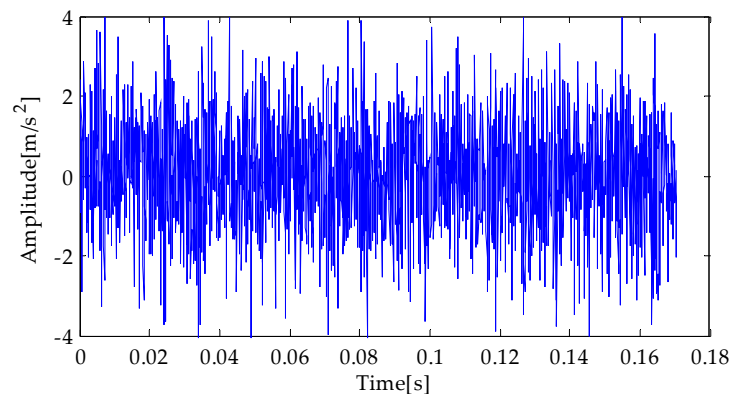


**Figure 35.** Time domain waveform of the mixed signal.

Next, Fourier decomposition method (FDM) analysis was conducted on the mixed signals containing noise due to inner race faults. Through signal decomposition, we

obtained 24 signal components and the final residual component. Due to space limitations, only the decomposition results of the first 20 signal components are presented in Figure 36. Upon observing the waveforms of these component signals, it is evident that this method effectively suppresses modal aliasing, thereby avoiding interference between different frequency components. Furthermore, endpoint effects were essentially eliminated.

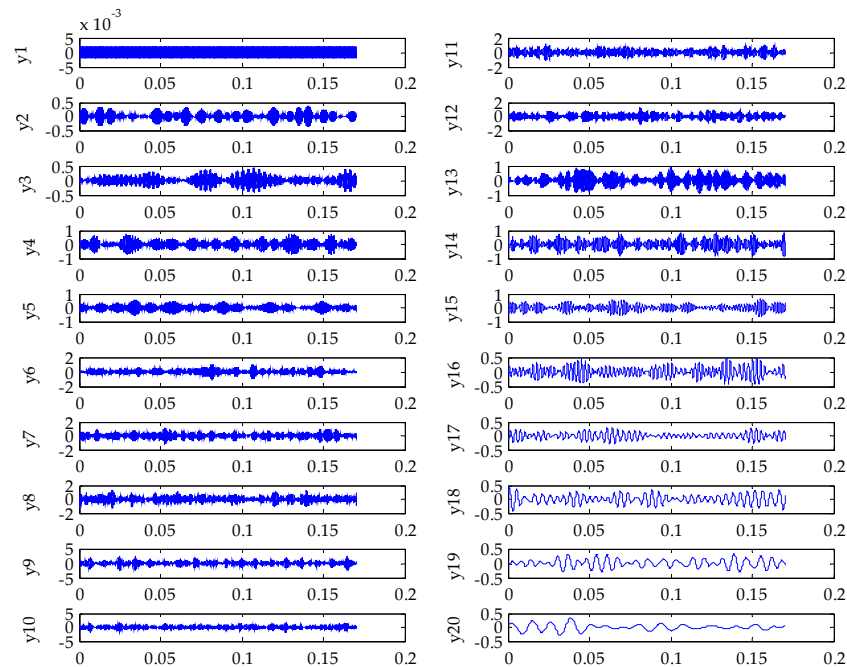


Figure 36. FDM decomposition result.

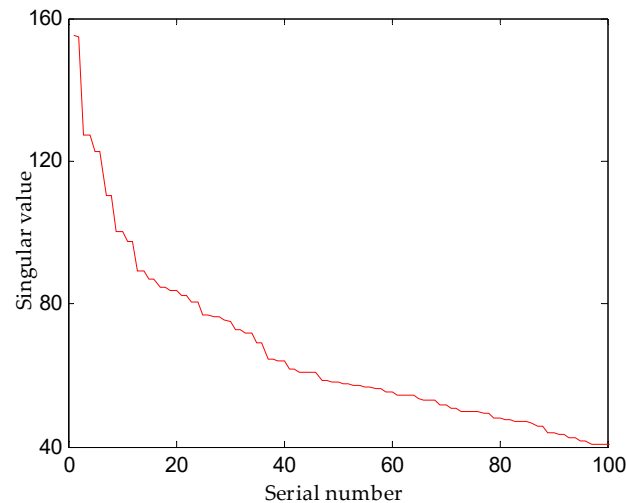
Following this, an in-depth statistical analysis was conducted on each signal component, which involved computing their kurtosis, skewness, and permutation entropy. Through these computations, we further derived filtering indices for each signal component. The detailed results of filtering index calculations for all signal components are provided in Table 9. Upon careful comparison of the filtering index values for these 24 signal components, it becomes evident that the 8th and 9th signal components exhibit significantly higher filtering index values compared to the other components. This suggests that these two signal components hold a more prominent position within the entire signal, potentially containing more significant fault information. Therefore, we selected these two signal components for signal reconstruction.

Table 9. Indicator result value (FDM).

	Y1	Y2	Y3	Y4	Y5	Y6	Y7	Y8	Y9	Y10
$\lambda$	0.728	1.481	1.673	1.832	1.891	2.266	2.225	2.503	2.598	2.144
	Y11	Y12	Y13	Y14	Y15	Y16	Y17	Y18	Y19	Y20
$\lambda$	2.241	2.187	2.141	2.056	2.017	1.886	1.772	1.679	1.593	1.953
	Y21	Y22	Y23	Y24						
$\lambda$	1.597	1.076	0.000	1.597						

Subsequently, through signal reconstruction based on the FDM algorithm and the constructed filtering rules, we further developed a Hankel matrix and subjected it to SVD decomposition. This process yielded the singular value spectrum and the singular value energy difference spectrum, as shown in Figures 37 and 38, respectively. The singular value energy difference spectrum in Figure 38 reveals disparities in energy between singular

values. Upon careful examination of this graph, it was observed that the energy at the 36th peak of the signal was relatively prominent, while all subsequent peaks exhibited comparatively lower energy. Based on this observation, we selected the reconstruction order corresponding to the 36th peak.



**Figure 37.** Signal singular value distribution curve.

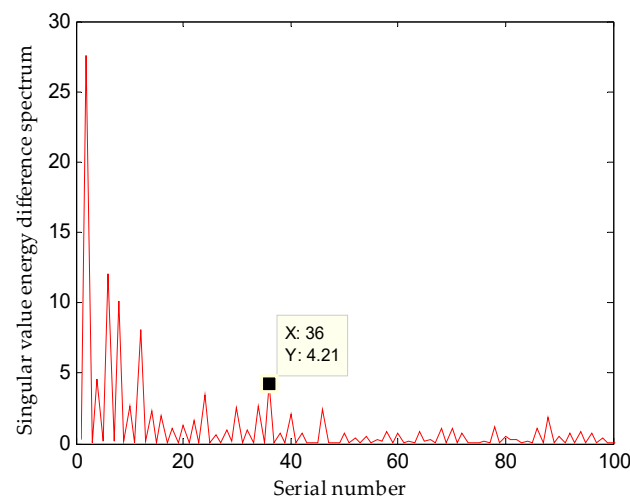


**Figure 38.** Singular value energy difference spectrum.

Figure 39 displays the time-domain waveform of the signal after denoising using the SVD method. It is evident from the figure that the originally embedded noise interference in the signal has been suppressed, highlighting the impulsive components in the outer race bearing fault signal. Figure 40, obtained through the Hilbert transform, represents the envelope spectrum. From this, the fundamental frequency, second harmonic, and third harmonic components of the outer race bearing fault can be clearly observed, allowing for the identification of the fault. However, it is worth noting that the peak frequencies of the fault are relatively low, and there are also many other irrelevant interferences present in the envelope spectrum, which may pose a certain level of difficulty in identifying the fault harmonics.

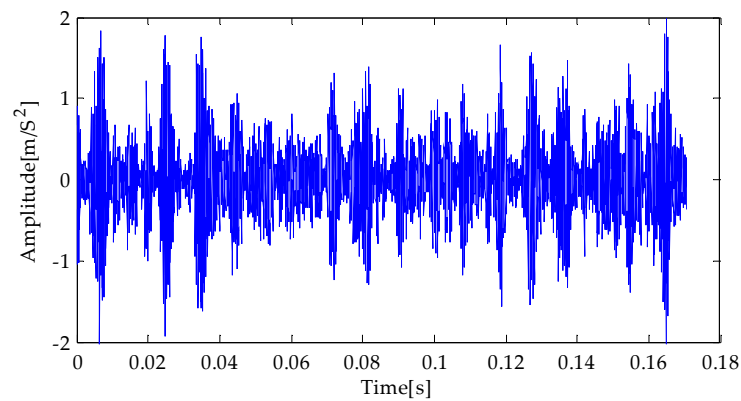


Figure 39. Signal after SVD denoising.

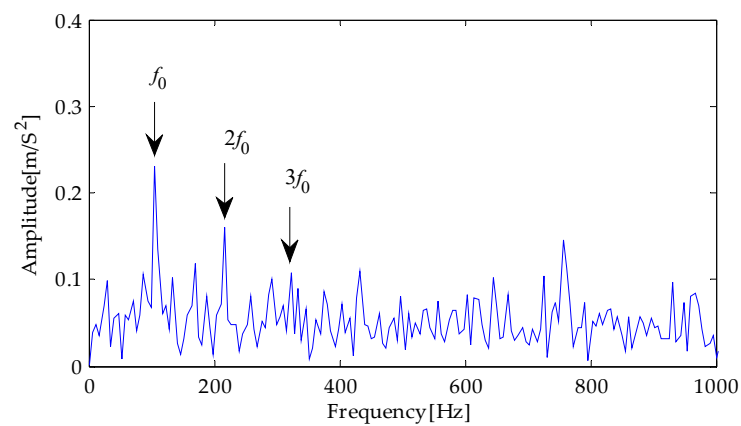


Figure 40. Envelope spectrum based on FDM-SVD.

To highlight the periodic impulsive features in the signal, the denoised signal (processed via the FDM-SVD method) was input into the CYCBD filter for precise fault feature extraction. Subsequently, an envelope spectrum was generated through the Hilbert transform, as shown in Figure 41. Upon careful examination of this figure, it is evident that after CYCBD filtering, the resulting envelope spectrum distinctly extracts multiple components, including the fault characteristic frequency and its second to sixth harmonics. These components are presented in the form of prominent peaks in the graph, facilitating observation and identification. Simultaneously, the CYCBD filtering process effectively suppresses surrounding interference components, thereby minimizing the impact on the recognition of harmonics.

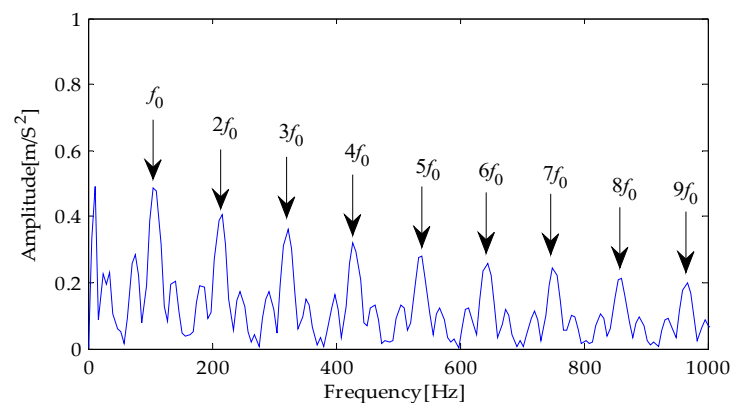


Figure 41. Envelope spectrum of CYCBD filter signal based on FDM-SVD.

Deconvolution techniques exhibit significant application value in the field of rotating machinery fault detection, particularly in extracting fault features from bearing vibration signals. This technology effectively extracts fault impact information from complex vibration signals of damaged mechanical components, thereby enhancing the amplitude of fault impacts and providing a robust basis for fault diagnosis. Among various deconvolution algorithms, MED, OMEDA, and MCKD each possess unique characteristics [22,38,39]. However, these algorithms have limitations to varying degrees in their applications. For instance, MED aims to maximize the kurtosis of the filtered signal, but it is susceptible to singular strong random pulses, potentially leading to deviations in diagnostic results. Similarly, OMEDA targets the maximization of the D-norm of the filtered signal and also faces interference from strong random pulses. Although the MCKD algorithm, which aims to maximize the correlated kurtosis of the filtered signal, improves diagnostic accuracy to a certain extent, it struggles to obtain a global optimal solution and can only extract a limited number of local pulses, thereby limiting its application scope. In contrast, the CYCBD algorithm aims to maximize the second-order cyclostationarity of the filtered signal, enabling it to better reflect the actual operating condition of the machinery. Compared to other deconvolution algorithms, the CYCBD algorithm typically results in larger amplitude values in the time–frequency domain after processing bearing vibration signals, facilitating more accurate identification of bearing fault characteristics. In the experiments conducted in this section, the CYCBD algorithm demonstrated superior performance in extracting the fault characteristic frequencies and their harmonics of the inner and outer rings of rolling bearings.

## 6. Conclusions

This paper investigates a combined approach for analyzing the feature extraction and fault diagnosis of noise-induced interference in rolling bearing signals. The research findings are summarized as follows:

- (1) By adopting the FDM to deeply process the original signal, we have successfully overcome the two major challenges of mode-mixing and endpoint effects commonly encountered in traditional methods. Compared to traditional techniques, the FDM's decomposed signal components more accurately reveal the hidden useful information in the original signal, providing more reliable data support for subsequent fault diagnosis.
- (2) By integrating multi-dimensional information, including kurtosis, skewness, and permutation entropy of signal components, we have constructed an efficient selection criterion to accurately identify the optimal signal component. Additionally, leveraging the excellent noise reduction capabilities of the SVD method, we have effectively mitigated the interference of background noise and improved signal quality. In comparison to experiments with methods such as EMD-SVD, EEMD-SVD, ITD-SVD, and VMD-SVD, the method proposed in this paper has demonstrated significant advantages in noise reduction evaluation metrics.
- (3) After successfully denoising the signal using SVD, we employed the CYCBD filtering method for fault feature separation, significantly enhancing the recognition capability for cyclic impulse components. Through simulation experiments and practical applications on rolling bearings, the fault feature extraction method introduced in this paper not only accurately captured the envelope spectra of fault frequencies and their harmonics but also exhibited clear advantages compared to traditional time–frequency analysis methods like EMD, EEMD, ITD, and VMD, as well as conventional deconvolution techniques such as MED, OMEDA, and MCKD. This comprehensively demonstrates the superiority and practicality of our proposed approach.

**Funding:** This research was funded by the Yunnan Fundamental Research Projects (No. 202301AT070256), the Training Program for Baoshan Xingbao Talents (No. 202303), and the 10th batch of Baoshan young and middle-aged leaders training academic and technical project (No. 202109).

**Data Availability Statement:** Data are contained with the article.

**Conflicts of Interest:** The author declares no conflicts of interest.

## References

1. Yang, J.; Zhou, D.H.; Liu, H. Optimal IMF Selection and Unknown Fault Feature Extraction for Rolling Bearings with Different Defect Modes. *Measurement* **2020**, *157*, 107660. [[CrossRef](#)]
2. Deng, M.; Deng, A.; Zhu, J.; Zhai, Y.; Liu, Y. Bandwidth Fourier Decomposition and Its Application in Incipient Fault Identification of Rolling Bearings. *Meas. Sci. Technol.* **2019**, *31*, 015012. [[CrossRef](#)]
3. Liu, W.; Chen, W.; Zhang, Z. A Novel Fault Diagnosis Approach for Rolling Bearing Based on High-Order Synchrosqueezing Transform and Detrended Fluctuation Analysis. *IEEE Access* **2020**, *8*, 12533–12541. [[CrossRef](#)]
4. Deutsch, D. *Nonlinear Time Series: Nonparametric and Parametric Methods*; Springer: New York, NY, USA, 2003.
5. Yu, F.T.S.; Lu, G. Short-Time Fourier Transform and Wavelet Transform with Fourier-Domain Processing. *Appl. Opt.* **1994**, *33*, 5262. [[CrossRef](#)]
6. Griffin, D.; Lim, J. Signal Estimation from Modified Short-Time Fourier Transform. *IEEE Trans. Acoust. Speech Signal Process.* **1984**, *32*, 236–243. [[CrossRef](#)]
7. Huang, N.E.; Shen, Z.; Long, S.R.; Wu, M.C.; Shih, H.H.; Zheng, Q.; Yen, N.C.; Tung, C.C.; Liu, H.H. The Empirical Mode Decomposition and the Hilbert Spectrum for Nonlinear and Non-Stationary Time Series Analysis. *Proc. R. Soc. London. Ser. A Math. Phys. Eng. Sci.* **1998**, *454*, 903–995. [[CrossRef](#)]
8. Smith, J.S. The Local Mean Decomposition and Its Application to EEG Perception Data. *J. R. Soc. Interface* **2005**, *2*, 443–454. [[CrossRef](#)] [[PubMed](#)]
9. Wu, Z.; Huang, N.E. Ensemble Empirical Mode Decomposition: A Noise-Assisted Data Analysis Method. *Adv. Adapt. Data Anal.* **2009**, *1*, 1–41. [[CrossRef](#)]
10. Singh, P.; Joshi, S.D.; Patney, R.K.; Saha, K. The Fourier Decomposition Method for Nonlinear and Non-Stationary Time Series Analysis. *Proc. R. Soc. A Math. Phys. Eng. Sci.* **2017**, *473*, 20160871. [[CrossRef](#)]
11. Parmar, K.S.; Kumar, A.; Kalita, U. ECG Signal Based Automated Hypertension Detection Using Fourier Decomposition Method and Cosine Modulated Filter Banks. *Biomed. Signal Process. Control* **2022**, *76*, 103629. [[CrossRef](#)]
12. Dou, C.; Lin, J. Extraction of Fault Features of Machinery Based on Fourier Decomposition Method. *IEEE Access* **2019**, *7*, 183468–183478. [[CrossRef](#)]
13. Deng, M.; Deng, A.; Zhu, J.; Shi, Y.; Liu, Y.; Chen, Q. Resonance-Based Bandwidth Fourier Decomposition Method for Gearbox Fault Diagnosis. *Meas. Sci. Technol.* **2021**, *32*, 035003. [[CrossRef](#)]
14. Fatimah, B.; Singh, P.; Singhal, A.; Pachori, R.B. Hand Movement Recognition from sEMG Signals Using Fourier Decomposition Method. *Biocybern. Biomed. Eng.* **2021**, *41*, 690–703. [[CrossRef](#)]
15. Guo, M.; Li, W.; Yang, Q.; Zhao, X.; Tang, Y. Amplitude Filtering Characteristics of Singular Value Decomposition and Its Application to Fault Dating Machinery. *Measurement* **2020**, *154*, 107444. [[CrossRef](#)]
16. Cheng, T.; Wu, Y.; Luo, X. Feature Extraction and Classification Method of Mine Microseismic Signals Based on EWT-Hankel-SVD. *Chin. J. Sci. Instrum.* **2019**, *40*, 181–191. (In Chinese)
17. Ren, Y.; Liu, P.; Hu, L.; Huang, J.; Qiao, R.; Chen, H.; Li, X.; Huang, S. Research on Noise Reduction Method of Pressure Pulsation Signal of Draft Tube of Hydropower Unit Based on ALIF-SVD. *Shock Vib.* **2021**, *2021*, 5580319. [[CrossRef](#)]
18. Zhong, C.; Liu, Y.; Wang, J.S.; Li, Z. RBFNN Fault Diagnosis Method of Rolling Bearing Based on Improved Ensemble Empirical Mode Decomposition and Singular Value Decomposition. *IAENG Int. J. Comput. Sci.* **2022**, *162*, 108018.
19. Cheng, X.; Mao, J.; Li, J.; Zhao, H.; Rao, Z. An EEMD-SVD-LWT Algorithm for Denoising a Lidar Signal. *Measurement* **2021**, *168*, 108405. [[CrossRef](#)]
20. Buzzoni, M.; Antoni, J.; D’Elia, G. Blind Deconvolution Based on Cyclostationarity Maximization and Its Application to Fault Identification. *J. Sound Vib.* **2018**, *432*, 569–601. [[CrossRef](#)]
21. Zhang, Q.; Pan, H.; Fan, Q.; Xu, F.; Wu, Y. Research on Fault Extraction Method of CYCBD Based on Seagull Optimization Algorithm. *Shock Vib.* **2021**, *13*, 8552024. [[CrossRef](#)]
22. Wang, Z.; Zhou, J.; Du, W.; Lei, Y.; Wang, J. Bearing Fault Diagnosis Method Based on Adaptive Maximum Cyclostationarity Blind Deconvolution. *Mech. Syst. Signal Process.* **2022**, *162*, 108018. [[CrossRef](#)]
23. Zheng, J.; Cao, S.; Pan, H.; Ni, Q. cSpectral Envelope-Based Adaptive Empirical Fourier Decomposition Method and Its Application to Rolling Bearing Fault Diagnosis. *ISA Trans.* **2022**, *129*, 476–492. [[CrossRef](#)] [[PubMed](#)]
24. Zhao, Q.; Wang, J.; Yin, J.; Zhang, P.; Xie, Z. Peak Envelope Spectrum Fourier Decomposition Method and Its Application in Fault Diagnosis of Rolling Bearings. *Measurement* **2022**, *198*, 111450. [[CrossRef](#)]
25. Tripathi, P.; Kumar, A.; Komaragiri, R.; Kumar, M. Watermarking of ECG Signals Compressed Using Fourier Decomposition Method. *Multimed. Tools Appl.* **2022**, *81*, 19543–19557. [[CrossRef](#)]
26. Lei, Z.; Wang, F.; Li, C. A denoising method of partial discharge signal based on improved SVD-VMD. *IEEE Trans. Dielectr. Electr. Insul.* **2023**, *30*, 2107–2116. [[CrossRef](#)]
27. Miao, Y.; Bai, X.; Cao, Y.; Liu, Y.; Dai, F.; Wang, F.; Qi, L.; Dou, W. A novel short-term traffic prediction model based on SVD and ARIMA with blockchain in industrial internet of Things. *IEEE Internet Things J.* **2023**, *10*, 21217–21226. [[CrossRef](#)]

28. Benrhouma, O.; Alkhodre, A.B.; AlZahrani, A.; Namoun, A.; Bhat, W.A. Using Singular Value Decomposition and Chaotic Maps for Selective Encryption of Video Feeds in Smart Traffic Management. *Appl. Sci.* **2022**, *12*, 3917. [[CrossRef](#)]
29. Li, J.; Liu, Y.; Xiang, J. Optimal Maximum Cyclostationary Blind Deconvolution for Bearing Fault Detection. *IEEE Sens. J.* **2023**, *23*, 15975–15987. [[CrossRef](#)]
30. Yang, J.; Zhou, C.; Li, X.; Pan, A.; Yang, T. A Fault Feature Extraction Method Based on Improved VMD Multi-Scale Dispersion Entropy and TVD-CYCBD. *Entropy* **2023**, *25*, 277. [[CrossRef](#)]
31. Tang, J.; Zhou, J.; Liu, T.; Liu, X. Compound defects feature extraction method of rotate vector reducers based on optimized maximum second-order cyclostationarity blind deconvolution. *IEEE Sens. J.* **2023**, *23*, 30652–30667. [[CrossRef](#)]
32. Liu, Z.; Zhang, L.; Xiong, G. Multilevel Feature Extraction Method for Adaptive Fault Diagnosis of Railway Axle Box Bearing. *Shock Vib.* **2023**, *2023*, 4748423. [[CrossRef](#)]
33. Sacchi, M.D.; Velis, D.R.; Comínguez, A.H. Minimum entropy deconvolution with frequency-domain constraints. *Geophysics* **1994**, *59*, 938–945. [[CrossRef](#)]
34. McDonald, G.L.; Zhao, Q.; Zuo, M.J. Maximum correlated Kurtosis deconvolution and application on gear tooth chip fault detection. *Mech. Syst. Signal Process.* **2012**, *33*, 237–255. [[CrossRef](#)]
35. Wang, X.; Ma, J. Weak fault feature extraction of rolling bearing based on SVM and improved MOMEDA. *Math. Probl. Eng.* **2021**, *2021*, 9966078. [[CrossRef](#)]
36. Smith, W.A.; Randall, R.B. Rolling element bearing diagnostics using the Case Western Reserve University data: A benchmark-study. *Mech. Syst. Signal Process.* **2015**, *64*, 100–131. [[CrossRef](#)]
37. Xi, C.; Gao, Z. Fault Diagnosis of Rolling Bearings Based on WPE by Wavelet Decomposition and ELM. *Entropy* **2022**, *24*, 1423. [[CrossRef](#)] [[PubMed](#)]
38. Ma, J.; Liang, S. Research on Rolling-Element Bearing Composite Fault Diagnosis Methods Based on RLMD and SSA-CYCBD. *Processes* **2022**, *10*, 2208. [[CrossRef](#)]
39. Qin, L.; Yang, G.; Sun, Q. Maximum correlation Pearson correlation coefficient deconvolution and its application in fault diagnosis of rolling bearings. *Measurement* **2022**, *205*, 112162. [[CrossRef](#)]

**Disclaimer/Publisher’s Note:** The statements, opinions and data contained in all publications are solely those of the individual author(s) and contributor(s) and not of MDPI and/or the editor(s). MDPI and/or the editor(s) disclaim responsibility for any injury to people or property resulting from any ideas, methods, instructions or products referred to in the content.